Electrophysiological dynamics of cognitive control networks in human memory and replication across four experiments

Anup Das[1] and Vinod Menon[1,2,3]

Department of Psychiatry & Behavioral Sciences[1]
Department of Neurology & Neurological Sciences[2]
Wu Tsai Neurosciences Institute[3]
Stanford University School of Medicine
Stanford, CA 94305

Title: Electrophysiological dynamics of cognitive control networks in human memory and replication across four experiments

Abbreviated title: Electrophysiology of Cognitive Networks in Memory

Keywords: Human intracranial EEG, triple-network model, cognitive control, episodic memory, human insula, salience network, default-mode network, frontoparietal network

Author names and affiliations:

Anup Das, Department of Psychiatry & Behavioral Sciences, Stanford University School of Medicine, Stanford, CA 94305

Vinod Menon, Department of Psychiatry & Behavioral Sciences, Department of Neurology & Neurological Sciences, and Stanford Neurosciences Institute, Stanford University School of Medicine, Stanford, CA 94305

Corresponding author email address: a1das@stanford.edu, menon@stanford.edu

Conflict of interest statement: The authors declare no competing financial interests.

Acknowledgements

This research was supported by NIH grants NS086085 and MH126518. We are grateful to members of the UPENN-RAM consortia for generously sharing their unique iEEG data. We thank Dr. Byeongwook Lee for assistance with the figures. We acknowledge the computational resources and support provided by the Stanford Research Computing Center.

Abstract

Dynamic interactions between large-scale brain networks are thought to underpin human cognitive processes such as episodic memory formation, but their underlying electrophysiological dynamics are not known. The triple network model, highlighting the salience, default mode, and frontoparietal networks, are fundamental to this process. To unravel the electrophysiological mechanisms underlying these interactions, we utilized intracranial EEG from 177 participants across four memory experiments. Findings revealed directed information flow from the anterior insula node of the salience network to the default mode and frontoparietal networks, regardless of the nature of the tasks – whether they involved externally driven stimuli during encoding or internally governed processes during free recall. Moreover, this pattern of information transmission was observed irrespective of the activation or suppression states of network nodes. Crucially, results were replicated across four different memory experiments. Our study advances understanding of how coordinated neural network interactions underpin cognitive operations.

Introduction

Episodic memory, the cognitive process of encoding, storing, and retrieving personally experienced events, is essential for a variety of complex cognitive functions and everyday tasks (Dickerson & Eichenbaum, 2010; Düzel, Penny, & Burgess, 2010; Moscovitch, Cabeza, Winocur, & Nadel, 2016; Ranganath & Ritchey, 2012; Rugg & Vilberg, 2013; Rutishauser, Reddy, Mormann, & Sarnthein, 2021; Yonelinas, Ranganath, Ekstrom, & Wiltgen, 2019). A deeper understanding of the circuit mechanisms in control of episodic memory is crucial, not only for elucidating fundamental brain operations, but also for probing the pathophysiology of numerous neuropsychological disorders such as Alzheimer's disease and other forms of dementia (Dickerson & Eichenbaum, 2010; Grady, Furey, Pietrini, Horwitz, & Rapoport, 2001; Uhlhaas & Singer, 2006). The formation of episodic memory is a dynamic process, predicated on the interaction of large-scale brain networks. As postulated by Mesulam in 1990, the mechanisms underlying all memory systems are facilitated by a complex architecture of interconnected brain regions. One influential framework for understanding these operations is the triple network model of dynamic cognitive control, which focuses on three pivotal large-scale brain networks—the salience network (SN), the default mode network (DMN), and the frontoparietal network (FPN)—that cooperatively manage cognitively demanding tasks (Cai, Ryali, Pasumarthy, Talasila, & Menon, 2021; Menon, 2011, 2023).

Central to this model is the anterior insula (AI), a key node of the salience network, which is posited to detect and filter task-relevant information, thereby facilitating a rapid and efficient switch between the DMN and FPN in response to shifting task demands (Menon, 2015). However, despite the model's influence, its electrophysiological underpinnings remain under-explored, and its role in network dynamics associated with episodic memory formation is not known. Addressing this knowledge gap, our study seeks to investigate the electrophysiological foundations of the triple network model and examine the dynamic interactions of these networks during episodic memory formation. By doing so, we aim to illuminate its functional significance in the context of episodic memory formation and how control processes operate to shape human memory.

Influential theoretical models of human memory posit a key role for control processes in regulating hierarchical processes associated with episodic memory formation (Andermane, Joensen, & Horner, 2021; Atkinson & Shiffrin, 1968; Bastos et al., 2012; Kumaran & McClelland, 2012; Tulving, 2002). Despite their central role, the precise neurophysiological underpinnings of these control processes remain poorly elucidated. Better understanding of these neural mechanisms has the potential to provide an empirical foundation for longstanding theoretical models but could also enable novel insights into the interplay between different brain regions and networks during memory processing. Here we seek to uncover neural mechanisms, bridging the gap between abstract cognitive models and their neurophysiological correlates.

The SN, DMN, and FPN may each play unique and critical interactive roles in episodic memory formation (Menon, 2023). The SN, known for its role in identifying and filtering salient stimuli, may enable the individual to focus on pertinent aspects of the environment or task, thereby facilitating effective memory encoding (Menon & Uddin, 2010). The DMN, often active during internally focused cognitive processes, is implicated in various aspects of memory including

retrieval of past experiences, envisioning future events, and forming detailed episodic memory traces (Buckner, Andrews-Hanna, & Schacter, 2008; Fox & Raichle, 2007; Fox et al., 2005; Raichle, 2015; Smallwood et al., 2021). The FPN, on the other hand, may contribute to top-down cognitive control and attention regulation (Badre, Poldrack, Paré-Blagoev, Insler, & Wagner, 2005; Badre & Wagner, 2007; Helfrich & Knight, 2016; Jin, Olk, & Hilgetag, 2010; Simons & Spiers, 2003; Uncapher & Wagner, 2009; Wagner, Paré-Blagoev, Clark, & Poldrack, 2001; Wagner, Shannon, Kahn, & Buckner, 2005). It plays a key role in the encoding and retrieval of episodic memories by coordinating information processing and attentional focus between internally and externally directed tasks. Together, these three networks may aid in orchestrating the intricate process of episodic memory formation, each contributing their unique capacities to encode and recall memory experiences. However, their neurophysiological correlates in the human brain remain largely unknown.

Human functional magnetic resonance imaging (fMRI) studies have revealed a critical role for the salience network in regulating the engagement and disengagement of the DMN and FPN across diverse cognitive and affective tasks (Cai et al., 2016; Cai et al., 2021; Chen, Cai, Ryali, Supekar, & Menon, 2016; Sridharan, Levitin, & Menon, 2008). Notably, during attentionally demanding tasks, the AI node of the salience network demonstrates task-related activation, whereas DMN nodes are typically suppressed (Bressler & Menon, 2010; Kronemer et al., 2022; Raichle et al., 2001; Seeley et al., 2007). Distinct from the AI, DMN nodes are predominantly involved in internally-focused processes, such as autobiographical memory recall, self-referential judgements, and future planning (Buckner et al., 2008; Greicius et al., 2008; Greicius & Menon, 2004; Laufs et al., 2003; Raichle et al., 2001).

Our understanding of the dynamic network interactions during human cognition, especially those involving large-scale brain networks, is primarily informed by fMRI studies (Menon, 2011; Uddin, 2015). However, the temporal resolution of these studies, typically around two seconds, is a significant constraint. This impedes our understanding of real-time, millisecond-scale neural dynamics and underscores the need to explore these networks' interactions at time scales more pertinent to neural circuit dynamics. The difficulties involved in acquiring intracranial EEG (iEEG) data from multiple brain regions have made it challenging to elucidate the precise neural mechanisms underlying the functioning of large-scale networks. These challenges obscure our understanding of the dynamic temporal properties and causal interactions between the AI and other large-scale distributed networks during memory formation.

To address this gap, we leveraged iEEG data acquired during multiple memory experiments from the University of Pennsylvania Restoring Active Memory (UPENN-RAM) study (Solomon et al., 2019). The dataset includes depth recordings from 177 participants with implants in the AI, the posterior cingulate cortex (PCC)/precuneus and medial prefrontal cortex (mPFC) nodes of the DMN, and the dorsal posterior parietal cortex (dPPC) and middle frontal gyrus (MFG) nodes of the FPN. As the largest available human iEEG open-source dataset, this resource provides a unique and unprecedented opportunity to probe the dynamics of triple network interactions during multiple episodic memory tasks. Specifically, we investigated the neurophysiological underpinnings of the AI's dynamic network interactions with the DMN and FPN—two pivotal networks in human cognition. Additionally, in response to the reproducibility challenges currently confronting neuroscience research, we evaluated the consistency of these interactions

across four distinct memory experiments and eight task conditions, thus enhancing the robustness and reliability of our findings.

To address the challenges of replicability in human electrophysiology research using iEEG data (Mercier et al., 2022), we examined four episodic memory experiments spanning both verbal and spatial domains. The first experiment was a verbal free recall memory task (VFR) in which participants were presented with a sequence of words during the encoding period and asked to remember them for subsequent verbal recall. The second was a categorized verbal free recall task (CATVFR) in which participants were presented with a sequence of words during the encoding period and asked to remember them for subsequent verbal recall. The third involved a paired associates learning verbal cued recall task (PALVCR) in which participants were presented with a sequence of word-pairs during the encoding period and asked to remember them for subsequent verbal cued recall. The fourth was a water maze spatial memory task (WMSM) in which participants were shown objects in various locations during the encoding periods and asked to retrieve the location of the objects during a subsequent recall period. This comprehensive approach afforded a rare opportunity in an iEEG setting to examine network interactions between the AI and the DMN and FPN nodes during both encoding and recall phases across multiple memory domains.

We determined directed causal information flow between the AI and the DMN and FPN during episodic memory formation. The AI is consistently engaged during attentional tasks and, dynamic causal modeling of fMRI data suggests that it exerts strong causal influences on the DMN and FPN in these contexts (Cai et al., 2016; Cai et al., 2021; Chen et al., 2016; Sridharan et al., 2008; Wen, Liu, Yao, & Ding, 2013). However, it remains unknown whether the AI plays a causal role during memory formation and whether such influences have a neurophysiological basis. To investigate the directionality of information flow between neural signals in the AI and DMN and FPN, we employed phase transfer entropy (PTE), a robust and powerful measure for characterizing information flow between brain regions based on phase coupling (Hillebrand et al., 2016; Lobier, Siebenhühner, Palva, & Matias, 2014; Wang et al., 2017). Crucially, it captures linear and nonlinear intermittent and nonstationary causal dynamics in iEEG data (Hillebrand et al., 2016; Lobier et al., 2014; Menon et al., 1996). We hypothesized that the AI would exert higher directed causal influence on the DMN and FPN than the reverse.

To further enhance our understanding of the dynamic activations within the three networks during episodic memory formation, we determined whether high-gamma band power in the AI, DMN, and FPN nodes depends on the phase of memory formation. Memory encoding, driven primarily by external stimulation, might invoke different neural responses compared to memory recall, which is more internally driven (Andrews-Hanna, 2012; Buckner et al., 2008). We hypothesized that DMN power would be suppressed during memory encoding as it is primarily driven by external stimuli, whereas an opposite pattern would be observed during memory recall which is more internally driven. Based on the distinct functions of the DMN and FPN—internally-oriented cognition and adaptive external response —we expected to observe differential modulations during encoding and recall phases. By testing these hypotheses, we aimed to provide a more detailed understanding of the dynamic role of triple network interactions in episodic memory formation, offering insights into the temporal dynamics and causal interactions within these large-scale cognitive networks.

Our next main objective was to investigate the replicability of our findings across multiple episodic memory domains involving both verbal and spatial materials. Reproducing findings across experiments is a significant challenge in neuroscience, particularly in invasive iEEG studies where data sharing and sample sizes have been notable limitations. There have been few previous replicated findings from human iEEG studies across multiple task domains. Quantitatively rigorous measures are needed to address the reproducibility crisis in human iEEG studies. We used Bayesian analysis to quantify the degree of replicability (Ly, Etz, Marsman, & Wagenmakers, 2019; Verhagen & Wagenmakers, 2014). Bayes factors (BFs) are a powerful tool for evaluating evidence for replicability of findings across tasks and for determining the strength of evidence for the null hypothesis (Verhagen & Wagenmakers, 2014). Briefly, the replication BF is the ratio of marginal likelihood of the replication data, given the posterior distribution estimated from the original data, and the marginal likelihood for the replication data under the null hypothesis of no effect (Ly et al., 2019). We computed the replication BF across the verbal and spatial memory domains.

Our analysis reveals novel insights into the neurophysiological basis of the interactions between large-scale cognitive control networks during memory encoding and recall across multiple stimulus types. Reliable and reproducible findings advance our understanding of the neural mechanisms that underpin human episodic memory and cognitive control, shedding light on how the brain effectively integrates information from distinct networks to support learning and memory formation.

Results

AI response compared to PCC/precuneus during encoding and recall in the VFR task

We first examined neuronal activity in the AI and the PCC/precuneus and tested whether activity in the PCC/precuneus is suppressed compared to activity in the AI. Previous studies have suggested that power in the high-gamma band (80-160 Hz) is correlated with fMRI BOLD signals (Hermes, Nguyen, & Winawer, 2017; Hutchison, Hashemi, Gati, Menon, & Everling, 2015; Lakatos, Gross, & Thut, 2019; Leopold, Murayama, & Logothetis, 2003; Mantini, Perrucci, Del Gratta, Romani, & Corbetta, 2007; Schölvinck, Maier, Ye, Duyn, & Leopold, 2010), and is thought to reflect local neuronal activity (Canolty & Knight, 2010). Therefore, we compared high-gamma band power (see **Methods** for details) in the AI and PCC/precuneus electrodes during both encoding and recall and across the four episodic memory tasks. Briefly, in the VFR task, participants were presented with a sequence of words and asked to remember them for subsequent recall (**Methods**, **Tables S1, S2a, S3a**, **Figures 1a, 2**).

Encoding Compared to the AI, high-gamma power in PCC/precuneus was suppressed during almost the entire window 110 – 1600 msec during memory encoding ($ps < 0.05$, **Figure 3a**).

Recall In contrast, suppression of high-gamma power in the PCC/precuneus was absent during the recall periods. Rather, high-gamma power in the PCC/precuneus was enhanced compared to the AI mostly during the 1390 – 1530 msec window prior to recall ($ps < 0.05$, **Figure 3a**).

AI response compared to PCC/precuneus during encoding and recall in the CATVFR task

We next examined high-gamma power in the CATVFR task. In this task, participants were presented with a list of words with consecutive pairs of words from a specific category (for example, JEANS-COAT, GRAPE-PEACH, etc.) and subsequently asked to recall as many as possible from the original list (**Methods**, **Tables S1, S2b, S3b**, **Figure 1b**) (Qasim, Mohan, Stein, & Jacobs, 2023).

Encoding High-gamma power in PCC/precuneus was suppressed compared to the AI during the 570 – 790 msec interval (*ps* < 0.05, **Figure 3b**).

Recall High-gamma power mostly did not differ between AI and PCC/precuneus prior to recall (*ps* > 0.05, **Figure 3b**).

AI response compared to PCC/precuneus during encoding and recall in the PALVCR task

The PALVCR task also consisted of three periods: encoding, delay, and recall (**Methods**, **Tables S1, S2c, S3c**, **Figure 1c**). During encoding, a list of word-pairs was visually presented, and then participants were asked to verbally recall the cued word from memory during the recall periods.

Encoding High-gamma power in PCC/precuneus was suppressed compared to the AI during the memory encoding period, during the 470 – 950 msec and 2010 – 2790 msec windows (*ps* < 0.05, **Figure 3c**).

Recall High-gamma power mostly did not differ between AI and PCC/precuneus prior to recall (*ps* > 0.05, **Figure 3c**).

AI response compared to PCC/precuneus during encoding and recall in the WMSM task

We next examined high-gamma power in the WMSM task. Participants performed multiple trials of a spatial memory task in a virtual navigation paradigm (Goyal et al., 2018; Jacobs et al., 2016; Lee et al., 2018) similar to the Morris water maze (Morris, 1984) (**Methods**, **Tables S1, S2d, S3d**, **Figure 1d**). Participants were shown objects in various locations during the encoding periods and asked to retrieve the location of the objects during the recall period.

Encoding High-gamma power in PCC/precuneus was suppressed compared to the AI, mostly during the 1390 – 2030 msec and 3150 – 4690 msec window (*ps* < 0.05, **Figure 3d**).

Recall High-gamma power mostly did not differ between AI and PCC/precuneus (*ps* < 0.05, **Figure 3d**).

Replication of increased high-gamma power in AI compared to PCC/precuneus across four memory tasks

We next used replication BF analysis to estimate the degree of replicability of high-gamma power suppression of the PCC/precuneus compared to the AI during the memory encoding

periods of the four tasks. We used the posterior distribution obtained from the VFR (primary) dataset as a prior distribution for the test of data from the CATVFR, PALVCR, and WMSM (replication) datasets (Ly et al., 2019) (see **Methods** for details). We used the encoding time-windows for which we most consistently observed decrease of PCC/precuneus high-gamma power compared to the AI. These correspond to 110 – 1600 msec during the VFR task, 570 – 790 msec in the CATVFR task, 2010 – 2790 msec in the PALVCR task, and 3150 – 4690 msec in the WMSM task. We first averaged the high-gamma power across these strongest time-windows for each task and then used replication BF analysis to estimate the degree of replicability of high-gamma power suppression of the PCC/precuneus compared to the AI.

Findings corresponding to the high-gamma power suppression of the PCC/precuneus compared to AI were replicated in the PALVCR (BF 5.16e+1) and WMSM (BF 2.69e+8) tasks. These results demonstrate very high replicability of high-gamma power suppression of the PCC/precuneus compared to AI during memory encoding. The consistent suppression effect was localized only to the PCC/precuneus, but not to the mPFC node of the DMN or the dPPC and MFG nodes of the FPN (**Figures S1-S3**).

In contrast to memory encoding, a similar analysis of high-gamma power did not reveal a consistent pattern of increased high-gamma power in AI and suppression of the PCC/precuneus across the four tasks during memory recall (**Figure 3**).

AI and PCC/precuneus response during encoding and recall compared to resting baseline

We examined whether AI and PCC/precuneus high-gamma power response during the encoding and recall periods are enhanced or suppressed when compared to the baseline periods. High-gamma power in the AI was increased compared to the resting baseline during both the encoding and recall periods, and across all four tasks ($ps < 0.05$, **Figure 3**). This suggests an enhanced role for the AI during both memory encoding and recall compared to resting baseline.

In contrast, high-gamma power in the PCC/precuneus was reduced compared to the resting baseline in three tasks – VFR, PALVCR, and WMSM – providing direct evidence for PCC/precuneus suppression during memory encoding (**Figure 3**). We did not find any increased high-gamma power activity in the PCC/precuneus, compared to the baseline, during memory retrieval (**Figure 3**). These results provide evidence for PCC/precuneus suppression compared to both the AI and resting baseline, during externally triggered stimuli during encoding.

High-gamma power for other brain areas compared to resting baseline were not consistent across tasks (**Figures S1-S3**).

Causal information flow from the AI to the DMN during encoding

We next examined directed information flow from the AI to the PCC/precuneus and mPFC nodes of the DMN, during the memory encoding periods of the VFR task. We used phase transfer entropy (PTE) (Lobier et al., 2014) to evaluate causal influences from the AI to the PCC/precuneus and mPFC and vice-versa.

Directed information flow from the AI to the PCC/precuneus ($F(1, 264) = 59.36$, $p<0.001$, Cohen's $d = 0.95$) and mPFC ($F(1, 208) = 13.96$, $p<0.001$, Cohen's $d = 0.52$) were higher, than the reverse (**Figure 4a**).

Replication across three experiments with BF We used replication BF analysis to estimate the degree of replicability of direction of information flow across the four experiments (**Table 1a**, **Figures 4b-d**, also see **Supplementary Results** for detailed stats related to the CATVFR, PALVCR, and WMSM experiments). Findings corresponding to the direction of information flow between the AI and the PCC/precuneus during memory encoding were replicated all three tasks (BFs 9.31e+5, 1.44e+4, and 1.68e+18 for CATVFR, PALVCR, and WMSM respectively). Findings corresponding to the direction of information flow between the AI and mPFC during memory encoding were also replicated across all three tasks (BFs 4.10e+1, 8.78e+0, and 5.34e+5 for CATVFR, PALVCR, and WMSM respectively). This highly consistent pattern of results was not observed in any other frequency band. These results demonstrate very high replicability of directed information flow from the AI to the DMN nodes during memory encoding.

These results demonstrate robust directed information flow from the AI to the PCC/precuneus and mPFC nodes of the DMN during memory encoding.

Causal information flow from the AI to the DMN during recall

Next, we examined causal influences of the AI on PCC/precuneus and mPFC during the recall phase of the verbal episodic memory task. During memory recall, directed information flow from the AI to the PCC/precuneus ($F(1, 264) = 43.09$, $p<0.001$, Cohen's $d = 0.81$) and mPFC ($F(1, 211) = 21.94$, $p<0.001$, Cohen's $d = 0.65$) were higher, than the reverse (**Figure 4a**).

Replication across three experiments with BF We next repeated the replication BF analysis for the recall periods of the memory tasks (**Table 1b**, **Figures 4b-d**, also see **Supplementary Results** for detailed stats related to the CATVFR, PALVCR, and WMSM experiments). Findings corresponding to the direction of information flow between the AI and the PCC/precuneus during memory recall were replicated across all three tasks (BFs 1.30e+5, 6.74e+0, and 2.54e+10 for CATVFR, PALVCR, and WMSM respectively). Findings corresponding to the direction of information flow between the AI and the mPFC during memory recall were also replicated across the CATVFR and WMSM tasks (BFs 2.02e+1 and 1.32e+4 respectively).

These results demonstrate very high replicability of directed information flow from the AI to the DMN nodes across verbal and spatial memory tasks, during both memory encoding and recall.

Causal information flow from AI to FPN nodes during memory encoding

We next probed directed information flow between the AI and FPN nodes during the encoding periods of the verbal free recall task. Directed information flow from the AI to the dPPC ($F(1, 1143) = 11.69$, $p<0.001$, Cohen's $d = 0.20$) and MFG ($F(1, 1245) = 21.69$, $p<0.001$, Cohen's $d = 0.26$) were higher, than the reverse during memory encoding of the VFR task (**Figure 5a**).

Replication across three experiments with BF We used replication BF analysis for the replication of AI causal influences on FPN nodes during the encoding phase of the memory tasks (**Table 1a, Figures 5b-d**). Similarly, we also obtained very high BFs for findings corresponding to the direction of information flow between the AI and dPPC (BFs > 2.33e+26) and also between the AI and MFG (BFs > 2.35e+27), across all three tasks.

These results demonstrate that the AI has robust directed information flow to the dPPC and MFG nodes of the FPN during memory encoding.

Causal information flow from AI to FPN nodes during memory recall

Directed causal influences from the AI to the dPPC ($F(1, 1143) = 17.47$, $p<0.001$, Cohen's $d = 0.25$) and MFG ($F(1, 1246) = 42.75$, $p<0.001$, Cohen's $d = 0.37$) were higher, than the reverse during memory recall of the VFR task (**Figure 5a**).

Replication across three experiments with BF We also found very high BFs for findings corresponding to the direction of information flow between the AI and the dPPC (BFs > 4.51e+27) and MFG (BFs > 6.90e+27) nodes of the FPN across the CATVFR, PALVCR, and WMSM tasks, during the memory recall period (**Table 1b, Figures 5b-d**).

These results demonstrate very high replicability of directed information flow from the AI to the FPN nodes across multiple memory experiments, during both memory encoding and recall.

Differential causal information flow from the AI to the DMN and FPN during episodic memory processing compared to resting baseline

We next examined whether differential causal directed information flow from the AI to the DMN and FPN nodes during the memory tasks differed from resting baseline. Resting baselines were extracted for each trial and the duration of task and rest epochs were matched to ensure that differences in network dynamics could not be explained by the differences in the duration of the epochs. We did not find any consistent directed causal influences from the AI on the DMN and FPN during memory encoding and recall, when compared to the resting baseline (**Figures S4, S5**). These findings suggest that the AI has higher directed causal influence on both the DMN and FPN nodes than the reverse regardless of task-related increase or decrease of its causal influence compared to the resting baseline.

Causal outflow hub during encoding and recall

fMRI studies have suggested that the AI acts as a causal outflow hub with respect to interactions with the DMN and FPN (Sridharan et al., 2008). To test the potential neural basis of this finding, we calculated net causal outflow as the difference between the total outgoing information and total incoming information (PTE(out)–PTE(in), see **Methods** for details).

Encoding This analysis revealed that the net causal outflow from the AI is positive and higher than the PCC/precuneus ($F(1, 3319) = 154.8$, $p<0.001$, Cohen's $d = 0.43$) node of the DMN, in the VFR task (**Figure 6a**).

This analysis also revealed that the net causal outflow from the AI is higher than both the dPPC ($F(1, 5346) = 67.87$, $p<0.001$, Cohen's $d = 0.23$) and MFG ($F(1, 6920) = 132.74$, $p<0.001$, Cohen's $d = 0.28$) nodes of the FPN, in the VFR task (**Figure 6a**).

Findings in the VFR task were also replicated across the CATVFR, PALVCR, and WMSM tasks, where we found that the net causal outflow from the AI is higher than the PCC/precuneus and mPFC nodes of the DMN and the dPPC and MFG nodes of the FPN (**Figures 6b-d**, also see **Supplementary Results** for detailed stats related to the CATVFR, PALVCR, and WMSM experiments).

Recall Net causal outflow from the AI is positive and higher than both PCC/precuneus ($F(1, 3287) = 151.21$, $p<0.001$, Cohen's $d = 0.43$) and mPFC ($F(1, 4694) = 7.81$, $p<0.01$, Cohen's $d = 0.08$) during the recall phase of the VFR task (**Figure 6a**).

Net causal outflow from the AI is also higher than both the dPPC ($F(1, 5388) = 90.71$, $p<0.001$, Cohen's $d = 0.26$) and MFG ($F(1, 6945) = 167.14$, $p<0.001$, Cohen's $d = 0.31$) nodes of the FPN during recall (**Figure 6a**).

Crucially, these findings were also replicated across the CATVFR, PALVCR, and WMSM tasks and during both encoding and recall periods (**Figures 6b-d**, also see **Supplementary Results** for detailed stats related to the CATVFR, PALVCR, and WMSM experiments). Together, these results demonstrate that the AI is a causal outflow hub in its interactions with the PCC/precuneus and mPFC nodes of the DMN and also the dPPC and MFG nodes of the FPN, during both verbal and spatial memory encoding and recall.

Discussion

Our research sought to uncover the electrophysiological basis of directed information flow in three large-scale cognitive control networks in relation to episodic memory formation. We focused on a triple network model comprising key cortical nodes of the salience, default mode (DMN) and frontoparietal (FPN) networks. We discovered that the AI node of the salience network exerts a strong causal influence on both the DMN and FPN during memory encoding as well as recall, extending the model's applicability beyond attention-demanding tasks to include memory-related tasks spanning verbal and spatial memory domains. Our findings advance understanding of the salience network's role in cognitive control processes engaged during episodic memory and highlight the importance of the triple network model in explaining the coordination of brain networks during various cognitive processes (**Figure 7**).

Dynamic causal interactions between the AI and the DMN and FPN are hypothesized to shape human cognition (Cai et al., 2016; Cai, Ryali, Chen, Li, & Menon, 2014; Dosenbach, Fair, Cohen, Schlaggar, & Petersen, 2008; Dosenbach et al., 2006; Menon, 2015; Menon & Uddin, 2010). Although fMRI research has suggested that the AI plays a pivotal role in the task-dependent engagement and disengagement of the DMN and FPN across diverse cognitive tasks (Menon & Uddin, 2010; Sridharan et al., 2008), the neuronal basis of these results or the possibility of their being artifacts arising from slow dynamics and regional variation in the

hemodynamic response inherent to fMRI signals remained unclear. To address these ambiguities, our analysis focused on casual interactions involving the AI and leveraged the high temporal resolution of iEEG signals. By investigating the directionality of information flow, we aimed to overcome the temporal resolution limitations of fMRI signals, providing a more mechanistic understanding of the AI's role in modulating the DMN and FPN during memory formation. To assess reproducibility, we scrutinized network interactions across four different episodic memory tasks involving verbal free recall, categorized verbal free recall, paired associates learning verbal cued recall, and water maze spatial episodic memory tasks (Solomon et al., 2019).

We employed Phase Transfer Entropy (PTE), a robust metric of nonlinear and nonstationary causal dynamics to investigate dynamic causal interactions between the AI and four key cortical nodes of the DMN and FPN. PTE assesses the ability of one time-series to predict future values of another, estimating time-delayed causal influences, and is superior to methods like phase locking or coherence as it captures nonlinear and nonstationary interactions (Bassett & Sporns, 2017; Hillebrand et al., 2016; Lobier et al., 2014). PTE offers a robust and powerful tool for characterizing information flow between brain regions based on phase coupling (Hillebrand et al., 2016; Lobier et al., 2014; Wang et al., 2017) and has been successfully utilized in our previous studies (Das, de Los Angeles, & Menon, 2022; Das & Menon, 2020, 2021, 2022b, 2023).

Informed by recent electrophysiology studies in nonhuman primates, which suggest that broadband field potentials activity, rather than narrowband, governs information flow in the brain (Davis, Muller, Martinez-Trujillo, Sejnowski, & Reynolds, 2020; Davis, Muller, & Reynolds, 2022), we first examined PTE in a 0.5 to 80 Hz frequency spectrum to assess dynamic causal influences of the AI on the DMN and FPN. Our analysis revealed that AI exerts stronger causal influences on the PCC/precuneus and mPFC nodes of the DMN than the reverse. A similar pattern also emerged for FPN nodes, with the AI displaying stronger causal influences on the dPPC and MFG, than the reverse. Crucially, this asymmetric pattern of directed causal information flow was replicated across all four memory tasks. Moreover, this pattern also held during the encoding and recall of memory phases of all four tasks. Consistent with our previous work (Das & Menon, 2020; Das, Myers, et al., 2022), a similar pattern of results was also observed in the low frequency delta-theta band. No consistent findings emerged in any of the other frequency bands.

Replication, a critical issue in all of systems neuroscience, is particularly challenging in the field of intracranial EEG studies, where data acquisition from patients is inherently difficult. Compounding this issue is the virtual absence of data sharing and the substantial complexities involved in collecting electrophysiological data across distributed brain regions (Das & Menon, 2022b). Consequently, one of our study's major objectives was to reproduce our findings across multiple experiments, bridging verbal and spatial memory domains and task phases. To quantify the degree of replicability of our findings across these domains, we employed replication Bayes Factor (BF) analysis (Ly et al., 2019; Verhagen & Wagenmakers, 2014). Our analysis revealed very high replication BFs related to replication of causal information flow from the AI to the DMN and FPN (**Table 1**). Specifically, the BFs associated with the replication of direction of information flow between the AI and the DMN and FPN were decisive (BFs > 100), demonstrating consistent results across various memory tasks and contexts.

These results reveal a consistent pattern of directed information flow between the AI and the DMN and FPN, which held true regardless of whether the tasks involved externally triggered stimuli during encoding and cued recall, or internally driven processes during free recall. This pattern underscores the robust and versatile role of the AI in modulating large-scale brain networks across diverse task contexts. In elucidating the interplay between externally and internally triggered memory processing, our study presents an intriguing finding. While we expected to observe a directed outflow from the AI during memory encoding triggered by external stimuli, the emergence of a similar pattern during internally triggered free recall was not initially foreseen. This reproducible pattern, observed across both externally and internally driven tasks, reinforces the crucial role of the AI in orchestrating network dynamics and advances our understanding of the intricate interplay between these large-scale networks in the human brain.

The PCC/precuneus and mPFC, which form the central nodes of the DMN, are typically deactivated during attention demanding tasks (Wen et al., 2013). However, these regions also play an important direct role in episodic memory (Buckner et al., 2008; Menon, 2023). In contrast, the dPPC and MFG nodes of the FPN, which are integral to cognitive control over memory, typically display heightened activity during memory tasks (Badre et al., 2005; Badre & Wagner, 2007; Wagner et al., 2001; Wagner et al., 2005). Our analysis of local neuronal activity substantiated a differential activity pattern, revealing a consistent suppression of high-gamma power in the PCC/precuneus compared to the AI during encoding periods across all four episodic memory tasks. Intriguingly, within the DMN, this suppression effect was confined to the PCC/precuneus, with no parallel reductions observed in the mPFC. Furthermore, we did not observe any significant differences in high-gamma band power between AI and the dPPC and MFG nodes of the FPN. Replication analysis using Bayesian techniques substantiated a high degree of replicability in the suppression of high-gamma power in the PCC/precuneus vis-à-vis the AI during memory encoding (BFs > 5.16e+1). These findings align with prior fMRI studies reporting DMN suppression during attention to external stimuli (Bressler & Menon, 2010; Raichle et al., 2001; Seeley et al., 2007) and are in line with research employing optogenetic stimulation of the AI in rodent brains that showcased dynamic DMN suppression patterns, particularly in the retrosplenial cortex (Menon et al., 2023). Our findings significantly extend this knowledge base to the specific domain of memory encoding, leveraging high-resolution iEEG recordings for temporal precision.

In contrast, our analysis of memory recall periods did not find a consistent pattern of increased high-gamma band power in AI and suppression of the PCC/precuneus across tasks.
These findings underscore a consistent and specific pattern of suppression in the PCC/precuneus high-gamma power that is reliably present during the encoding periods of episodic memory tasks, but absent during recall periods. The observed variance might stem from the differing cognitive demands—externally-stimulated effects during memory encoding versus internally-driven processes during free recall—characteristic of these two stages of memory.

High-gamma activity (typically ranging from 80-160 Hz) has been reliably implicated in various cognitive tasks across sensory modalities, including visual (Lachaux et al., 2005; Tallon-Baudry, Bertrand, Hénaff, Isnard, & Fischer, 2005), auditory (Crone, Boatman, Gordon, & Hao, 2001; Edwards, Soltani, Deouell, Berger, & Knight, 2005), and across cognitive domains, including

working memory (Canolty et al., 2006; Mainy et al., 2007) and episodic memory (Daitch & Parvizi, 2018; Sederberg et al., 2007). This increase in high-gamma band activity is indicative of localized, task-related neural processing, often correlating with the synchronized activity of local neural populations (Canolty & Knight, 2010). Specifically, increases in high-gamma power have been associated with elevated neuronal spiking and synaptic activity, rendering it a valuable marker of task-specific computations in local neuronal circuits (Ray, Crone, Niebur, Franaszczuk, & Hsiao, 2008). In our study, we observed a distinctive pattern of suppression in PCC/precuneus high-gamma activity during memory encoding phases, but not during recall, compared to resting baseline. We suggest that a functional down-regulation is a plausible explanation of this high gamma suppression. This task-specific suppression indicates that the PCC/precuneus may have a specialized role in the regulation of attentional resources during the encoding phase of episodic memory formation.

Notably, our findings reveal a robust and consistent causal influence exerted by the AI on all nodes of both the DMN and the FPN, extending across all four memory tasks and both memory encoding and recall phases. These causal influences were prominently manifest in broadband signals. Interestingly, such causal influences were not observed in the high-gamma frequency range (80-160 Hz). This absence aligns with current models positing that high-gamma activity is more likely to reflect localized processing, while lower-frequency bands are implicated in longer-range network communication and coordination (Bastos et al., 2015; Das, de Los Angeles, et al., 2022; Das & Menon, 2020, 2021, 2022b, 2023; K. J. Miller et al., 2007). More generally, our findings emphasize that it is crucial to differentiate between high-gamma activity (f > 80 Hz) and sub-high-gamma (f < 80 Hz) fluctuations, as these signal types are indicative of different underlying physiological processes, each with distinct implications for understanding neural network dynamics.

Our findings illuminate the interplay of large-scale brain networks in memory formation processes. The AI is considered a pivotal node in the triple network model of brain function, which encompasses the DMN and FPN, and the salience network. In this model, the AI, a key component of the salience network, is posited to act as a switch between the DMN and FPN. The investigation of activation (up-regulation) and deactivation (down-regulation) relative to the AI provides insights into the dynamics of how these large-scale networks interact during memory processes. More specifically, memory-related operations involve intricate interplays between different brain regions that are activated or deactivated depending on the stage of memory process— encoding or recall. By evaluating the causal influences of the AI, we were able to chart the direction and intensity of information flow within these networks, thereby elucidating whether the triple network control processes are also applicable to memory tasks.

Previous electrophysiology research exploring intrinsic (resting-state) dynamics employed single-pulse electrical stimulation to probe the causal cortical dynamics associated with the salience network in parallel with electrode recordings in either the DMN or the FPN (Shine et al., 2017). While the specific effect of AI stimulation was not examined, it was noted that stimulation of electrodes in the salience network, of which the AI is a major node, elicited a rapid (<70 ms) high-gamma band response, whereas stimulation of the DMN led to sustained responses in later time windows (85–200 ms). Delayed responses in high gamma band power have also been reported in the DMN, compared to the AI, during a Go/NoGo task (Kucyi et al.,

2020). However, the direction and magnitude of information flow between the AI and the DMN was not directly analyzed. Our analysis of causal dynamics and direction of information flow involving the AI and the DMN and FPN fills a critical gap in the electrophysiology literature pertaining to network interactions during episodic memory. Importantly, given the frequency-specific effects of electrical stimulation, which can often exhibit opposing excitatory and inhibitory impacts (Grover, Nguyen, & Reinhart, 2021; Huang & Keller, 2022; Mercier et al., 2022), causal influences associated with stimulation at a certain frequency may not necessarily mirror those occurring during task performance. Thus, our findings offer novel insights into the dynamic operation of cognitive control circuits during memory encoding and recall.

Beyond information flow along individual pathways linking the AI with the DMN and FPN, our PTE analysis further revealed that the AI is a causal outflow hub in its interactions with the DMN and the FPN regardless of stimulus materials. As a central node of the salience network (Menon & Uddin, 2010; Seeley et al., 2007; Sridharan et al., 2008), the AI is known to play a crucial role in influencing other networks (Menon & Uddin, 2010; Uddin, 2015). Our results align with findings based on control theory analysis of brain networks during a working memory task. Specifically, Cai et al found higher causal outflow and controllability associated with the AI compared to DMN and FPN nodes during an n-back working memory task (Cai et al., 2021). Controllability refers to the ability to perturb a system from a given initial state to other configuration states in finite time by means of external control inputs. Intuitively, nodes with higher controllability require lower energy for perturbing a system from a given state, making controllability measures useful for identifying driver nodes with the potential to influence overall state dynamics. By virtue of its higher controllability relative to other brain areas, the AI is well-positioned to dynamically engage and disengage with other brain areas. These findings expand our understanding of the AI's role, extending beyond attention and working memory tasks to incorporate two distinct stages of episodic memory formation. Our study, leveraging the temporal precision of iEEG data, substantially enhances previous fMRI findings by unveiling the neurophysiological mechanisms underlying the AI's dynamic regulation of network activity during memory formation and cognition more generally.

Our findings bring a novel perspective to the seminal model of human memory proposed by Atkinson and Shiffrin (Atkinson & Shiffrin, 1968). This model conceptualizes memory as a multistage process, with control mechanisms regulating the transition of information across these stages. The observed suppression of high-gamma power in the PCC/precuneus and enhancement in the AI during the encoding phase may be seen as one neurophysiological manifestation of these control processes. The AI's role as a dynamic switch, modulating activity between the DMN and FPN, aligns with active processing and control needed to encode sensory information into short-term memory. On the other hand, the transformations observed during the recall phase, particularly the discernable lack of DMN suppression patterns, may correspond to the retrieval processes where internally generated cues steer the reactivation of memory representations during recall. These results provide a novel neurophysiological model for understanding the complex control processes underpinning human memory functioning.

Limitations

Our study has some constraints worth noting. Three out of the four memory experiments examined – VFR, CATVFR, and PALVCR – involved verbal recall which likely involves stronger left-lateralized activation compared to non-verbal memory encoding (Golby et al., 2001; Kelley et al., 1998; Nagel, Herting, Maxwell, Bruno, & Fair, 2013; Thomason et al., 2009). Future studies with denser sampling of electrodes across both hemispheres and multiple verbal and non-verbal memory experiments are needed to separately examine the role of the individual hemispheres during verbal versus non-verbal memory retrieval. Additionally, our conclusions about the causal influence of the AI electrodes on the DMN and FPN electrodes were derived using computational methods. To more robustly establish these causal links, future studies should employ causal circuit manipulation techniques such as deep brain stimulation, using electrodes implanted in both the DMN and FPN while participants engage in episodic memory tasks. This would provide further empirical evidence for the role of the AI in modulating large-scale brain networks during human memory processing.

Conclusions

Our study sheds new light on the neural dynamics underpinning episodic memory processing in humans. Using high temporal resolution iEEG recordings, we assessed real-time neural signaling and causal network interactions between the anterior insula (AI), the default mode network (DMN), and the frontoparietal network (FPN) across a large cohort of participants engaged in four different episodic memory experiments. We discovered that the AI node of the salience network exerts a strong causal influence on both the DMN and FPN during memory encoding as well as retrieval periods, extending the model's applicability to episodic memory in both the verbal and spatial domains. Our results elucidate the AI's crucial role as a 'causal hub', modulating information flow within and between these cognitive control networks during two distinct stages of memory formation – encoding and recall.

The robust reproducibility of our findings across various memory tasks emphasizes the reliability and generalizability of our results, thus significantly expanding our understanding of the operational principles of dynamic circuit mechanisms in memory formation. More broadly, our results highlight signaling across distributed large-scale brain networks during episodic memory processing, reinforcing the concept that memory operations are reliant on the concerted action of an ensemble of widely distributed brain networks (Mesulam, 1990). Finally, our study not only advances understanding of neural circuit dynamics but also offers a template for examining how alterations in neural networks can influence memory performance in disorders like Alzheimer's disease, which are known to be intricately associated with dysfunctions in the salience, default mode, and frontoparietal networks (Bonthius, Solodkin, & Van Hoesen, 2005; Guzmán-Vélez et al., 2022). The insights gained from our work could potentially guide the development of targeted interventions for remediation and management of these memory-impairing disorders.

Figure Captions

Figure 1. Task design of the encoding and recall periods of the memory experiments, and iEEG recording sites in AI, with DMN and FPN nodes. (a) Experiment 1, Verbal free recall (VFR): (i) Task design of memory encoding and recall periods of the verbal free recall experiment (see **Methods** for details). Participants were first presented with a list of words in the encoding block and asked to recall as many as possible from the original list after a short delay. **(ii)** Electrode locations for AI with DMN nodes (top panel) and AI with FPN nodes (bottom panel), in the verbal free recall experiment. Proportion of electrodes for AI, PCC/Pr, mPFC, dPPC, and MFG were 9%, 8%, 19%, 32%, and 32% respectively, in the VFR experiment. **(b) Experiment 2, Categorized verbal free recall (CATVFR): (i)** Task design of memory encoding and recall periods of the categorized verbal free recall experiment (see **Methods** for details). Participants were presented with a list of words with consecutive pairs of words from a specific category (for example, JEANS-COAT, GRAPE-PEACH, etc.) in the encoding block and subsequently asked to recall as many as possible from the original list after a short delay. **(ii)** Electrode locations for AI with DMN nodes (top panel) and AI with FPN nodes (bottom panel), in the categorized verbal free recall experiment. Proportion of electrodes for AI, PCC/Pr, mPFC, dPPC, and MFG were 10%, 7%, 11%, 35%, and 37% respectively, in the CATVFR experiment. **(c) Experiment 3, Paired associates learning verbal cued recall (PALVCR): (i)** Task design of memory encoding and recall periods of the paired associates learning verbal cued recall experiment (see **Methods** for details). Participants were first presented with a list of 6 word-pairs in the encoding block and after a short post-encoding delay, participants were shown a specific word-cue and asked to verbally recall the cued word from memory. **(ii)** Electrode locations for AI with DMN nodes (top panel) and AI with FPN nodes (bottom panel), in the paired associates learning verbal cued recall experiment. Proportion of electrodes for AI, PCC/Pr, mPFC, dPPC, and MFG were 14%, 5%, 13%, 33%, and 35% respectively, in the PALVCR experiment. **(d) Experiment 4, Water maze spatial memory (WMSM): (i)** Task design of memory encoding and recall periods of the water maze spatial memory experiment (see **Methods** for details). Participants were shown objects in various locations during the encoding period and asked to retrieve the location of the objects during the recall period. Modified from Jacobs et. Al. (2018) with permission. **(ii)** Electrode locations for AI with DMN nodes (top panel) and AI with FPN nodes (bottom panel), in the water maze spatial memory experiment. Proportion of electrodes for AI, PCC/Pr, mPFC, dPPC, and MFG were 10%, 15%, 13%, 38%, and 24% respectively, in the WMSM experiment. Overall, proportion of electrodes for VFR, CATVFR, PALVCR, and WMSM experiments were 43%, 27%, 15%, and 15% respectively. AI: anterior insula, PCC: posterior cingulate cortex, Pr: precuneus, mPFC: medial prefrontal cortex, dPPC: dorsal posterior parietal cortex, MFG: middle frontal gyrus.

Figure 2. Anterior insula electrode locations (red) visualized on insular regions based on the atlas by Faillenot and colleagues (Faillenot, Heckemann, Frot, & Hammers, 2017). Anterior insula is shown in blue, and posterior insula mask is shown in green (see **Methods** for details). This atlas is based on probabilistic analysis of the anatomy of the insula with demarcations of the AI based on three short dorsal gyri and the PI which encompasses two long and ventral gyri.

Figure 3. iEEG evoked response, quantified using high-gamma (HG) power, for AI (red) and PCC/precuneus (blue) during (a) VFR, (b) CATVFR, (c) PALVCR, and (d) WMSM

experiments. Green horizontal lines denote high-gamma power for AI compared to PCC/precuneus (*ps* < 0.05). Red horizontal lines denote increase of AI response compared to the resting baseline during the encoding and recall periods (*ps* < 0.05). Blue horizontal lines denote decrease of PCC/precuneus response compared to the baseline during the encoding periods and increase of PCC/precuneus response compared to the baseline during the recall periods (*ps* < 0.05).

Figure 4. Causal directed information flow between the anterior insula and the PCC/precuneus and mPFC nodes of the default mode network (DMN), across verbal and spatial memory domains, measured using phase transfer entropy (PTE). (a) Experiment 1, VFR: The anterior insula showed higher causal directed information flow to the PCC/precuneus (AI → PCC/Pr) compared to the reverse direction (PCC/Pr → AI) (n=142) during both encoding and recall. The anterior insula also showed higher causal directed information flow to the mPFC (AI → mPFC) compared to the reverse direction (mPFC → AI) (n=112) during both memory encoding and recall. **(b) Experiment 2, CATVFR:** The anterior insula showed higher causal directed information flow to the PCC/precuneus (AI → PCC/Pr) compared to the reverse direction (PCC/Pr → AI) (n=46) during both encoding and recall. **(c) Experiment 3, PALVCR:** The anterior insula showed higher causal directed information flow to the PCC/precuneus (AI → PCC/Pr) compared to the reverse direction (PCC/Pr → AI) (n=10) during both encoding and recall. **(d) Experiment 4, WMSM:** The anterior insula showed higher causal directed information flow to PCC/precuneus (AI → PCC/Pr) than the reverse (PCC/Pr → AI) (n=91), during both spatial memory encoding and recall. The anterior insula also showed higher causal directed information flow to mPFC (AI → mPFC) than the reverse (mPFC → AI) (n=23), during both spatial memory encoding and recall. In each panel, the direction for which PTE is higher, is underlined. White dot in each violin plot represents median PTE across electrode pairs. *** $p < 0.001$, * $p < 0.05$.

Figure 5. Causal directed information flow between the anterior insula and the dPPC and MFG nodes of the frontoparietal network (FPN), across verbal and spatial memory domains. (a) Experiment 1, VFR: The anterior insula showed higher causal directed information flow to the dorsal PPC (AI → dPPC) compared to the reverse direction (dPPC → AI) (n=586) during both encoding and recall. The anterior insula also showed higher causal directed information flow to the MFG (AI → MFG) compared to the reverse direction (MFG → AI) (n=642) during both memory encoding and recall. **(b) Experiment 2, CATVFR:** The anterior insula showed higher causal directed information flow to the dorsal PPC (AI → dPPC) compared to the reverse direction (dPPC → AI) (n=327) during both encoding and recall. **(c) Experiment 3, PALVCR:** The anterior insula showed higher causal directed information flow to the dorsal PPC (AI → dPPC) compared to the reverse direction (dPPC → AI) (n=242) during both encoding and recall. The anterior insula also showed higher causal directed information flow to the MFG (AI → MFG) compared to the reverse direction (MFG → AI) (n=362) during memory recall. **(d) Experiment 4, WMSM:** The anterior insula showed higher causal directed information flow to MFG (AI → MFG) than the reverse (MFG → AI) (n=177), during both spatial memory encoding and recall. In each panel, the direction for which PTE is higher, is underlined. *** $p < 0.001$, ** $p < 0.01$.

Figure 6. The anterior insula is a causal outflow hub in its interactions with the DMN and FPN, during encoding and recall periods, and across memory experiments. In each panel, the net direction of information flow between the AI and the DMN and FPN nodes are indicated by green arrows on the right. *** $p < 0.001$, ** $p < 0.01$, * $p < 0.05$.

Figure 7. Schematic illustration of key findings related to the intracranial electrophysiology of the triple network model in human episodic memory. (a) High-gamma response: Our analysis of local neuronal activity revealed consistent suppression of high-gamma power in the PCC/precuneus compared to the AI during encoding periods across all four episodic memory experiments. We did not consistently observe any significant differences in high-gamma band power between AI and the mPFC node of the DMN or the dPPC and MFG nodes of the FPN during the encoding periods across the four episodic memory experiments. In contrast, we detected similar high-gamma band power in the PCC/precuneus relative to the AI during the recall periods. **(b) Directed information flow:** Despite variable patterns of local activation and suppression across DMN and FPN nodes during memory encoding and recall, we found stronger causal influence (denoted by green arrows, thickness of arrows denotes degree of replicability across experiments, see **Table 1**) by the AI on both the DMN as well as the FPN nodes than the reverse, across all four memory experiments, and during both encoding and recall periods.

Tables

Table 1. Replicability of findings of causal interactions of the AI with the DMN and FPN nodes for different memory experiments during (a) Memory Encoding and (b) Memory Recall. The verbal free recall (VFR) task was considered the original dataset and the categorized verbal free recall (CATVFR), paired associates learning verbal cued recall (PALVCR), and water maze spatial memory (WMSM) tasks were considered replication datasets and Bayes factor (BF) for replication was calculated for pairwise tasks (verbal free recall vs. T, where T can be categorized verbal free recall, paired associates learning verbal cued recall, or water maze spatial memory task). Significant BF results (BF>3) are indicated in bold. AI: anterior insula, PCC: posterior cingulate cortex, Pr: precuneus, mPFC: medial prefrontal cortex, dPPC: dorsal posterior parietal cortex, MFG: middle frontal gyrus.

(a) Memory Encoding

Finding	**Bayes Factor for VFR-CATVFR replication**	**Bayes Factor for VFR-PALVCR replication**	**Bayes Factor for VFR-WMSN replication**
AI → PCC/Pr > PCC/Pr → AI	**9.31e+5**	**1.44e+4**	**1.68e+18**
AI → mPFC > mPFC → AI	**4.10e+1**	**8.78e+0**	**5.34e+5**
AI → dPPC > dPPC → AI	**3.95e+43**	**2.33e+26**	**3.25e+40**
AI → MFG > MFG → AI	**1.49e+51**	**1.61e+33**	**2.35e+27**

(b) Memory Recall

Finding	**Bayes Factor for VFR-CATVFR replication**	**Bayes Factor for VFR-PALVCR replication**	**Bayes Factor for VFR-WMSN replication**
AI → PCC/Pr > PCC/Pr → AI	**1.30e+5**	**6.74e+0**	**2.54e+10**
AI → mPFC > mPFC → AI	**2.02e+1**	3.52e-5	**1.32e+4**
AI → dPPC > dPPC → AI	**7.04e+38**	**2.98e+45**	**4.51e+27**
AI → MFG > MFG → AI	**1.74e+54**	**5.72e+52**	**6.90e+27**

Methods

UPENN-RAM iEEG recordings

iEEG recordings from 249 patients shared by Kahana and colleagues at the University of Pennsylvania (UPENN) (obtained from the UPENN-RAM public data release) were used for analysis (Jacobs et al., 2016). Patients with pharmaco-resistant epilepsy underwent surgery for removal of their seizure onset zones. iEEG recordings of these patients were downloaded from a UPENN-RAM consortium hosted data sharing archive (URL: http://memory.psych.upenn.edu/RAM). Prior to data collection, research protocols and ethical guidelines were approved by the Institutional Review Board at the participating hospitals and informed consent was obtained from the participants and guardians (Jacobs et al., 2016).

Details of all the recordings sessions and data pre-processing procedures are described by Kahana and colleagues (Jacobs et al., 2016). Briefly, iEEG recordings were obtained using subdural grids and strips (contacts placed 10 mm apart) or depth electrodes (contacts spaced 5–10 mm apart) using recording systems at each clinical site. iEEG systems included DeltaMed XlTek (Natus), Grass Telefactor, and Nihon-Kohden EEG systems. Electrodes located in brain lesions or those which corresponded to seizure onset zones or had significant interictal spiking or had broken leads, were excluded from analysis.

Anatomical localization of electrode placement was accomplished by co-registering the postoperative computed CTs with the postoperative MRIs using FSL (FMRIB (Functional MRI of the Brain) Software Library), BET (Brain Extraction Tool), and FLIRT (FMRIB Linear Image Registration Tool) software packages. Preoperative MRIs were used when postoperative MRIs were not available. The resulting contact locations were mapped to MNI space using an indirect stereotactic technique and OsiriX Imaging Software DICOM viewer package.

We used the insula atlas by Faillenot and colleagues to demarcate the anterior insula (AI) (Faillenot et al., 2017), downloaded from http://brain-development.org/brain-atlases/adult-brain-atlases/. This atlas is based on probabilistic analysis of the anatomy of the insula with demarcations of the AI based on three short dorsal gyri and the posterior insula (PI) which encompasses two long gyri. To visualize iEEG electrodes on the insula atlas, we used surface-rendering code (GitHub: https://github.com/ludovicbellier/InsulaWM) provided by Llorens and colleagues (Llorens et al., 2023). We used the Brainnetome atlas (Fan et al., 2016) to demarcate the posterior cingulate cortex (PCC)/precuneus, the medial prefrontal cortex (mPFC), the dorsal posterior parietal cortex (dPPC), and the middle frontal gyrus (MFG). Out of 249 individuals, data from 177 individuals (aged from 16 to 64, mean age 36.3 ± 11.5, 91 females) were used for subsequent analysis based on electrode placement in the AI and the PCC/precuneus, mPFC, dPPC, and MFG.

Original sampling rates of iEEG signals were 500 Hz, 1000 Hz, 1024 Hz, and 1600 Hz. Hence, iEEG signals were downsampled to 500 Hz, if the original sampling rate was higher, for all subsequent analysis. The two major concerns when analyzing interactions between closely spaced intracranial electrodes are volume conduction and confounding interactions with the reference electrode (Burke et al., 2013; Frauscher et al., 2018). Hence bipolar referencing was

used to eliminate confounding artifacts and improve the signal-to-noise ratio of the neural signals, consistent with previous studies using UPENN-RAM iEEG data (Burke et al., 2013; Ezzyat et al., 2018). Signals recorded at individual electrodes were converted to a bipolar montage by computing the difference in signal between adjacent electrode pairs on each strip, grid, and depth electrode and the resulting bipolar signals were treated as new "virtual" electrodes originating from the midpoint between each contact pair, identical to procedures in previous studies using UPENN-RAM data (Solomon et al., 2019). Line noise (60 Hz) and its harmonics were removed from the bipolar signals and finally each bipolar signal was Z-normalized by removing mean and scaling by the standard deviation. For filtering, we used a fourth order two-way zero phase lag Butterworth filter throughout the analysis.

Episodic memory experiments

(a) Verbal free recall (VFR) task

Patients performed multiple trials of a verbal free recall experiment, where they were presented with a list of words and subsequently asked to recall as many as possible from the original list (**Figure 1a**) (Solomon et al., 2017; Solomon et al., 2019). The task consisted of three periods: encoding, delay, and recall. During encoding, a list of 12 words was visually presented for ~30 sec. Words were selected at random, without replacement, from a pool of high frequency English nouns (http://memory.psych.upenn.edu/Word_Pools). Each word was presented for a duration of 1600 msec, followed by an inter-stimulus interval of 800 to 1200 msec. After the encoding period, participants engaged in a math distractor task (the delay period in **Figure 1a**), where they were instructed to solve a series of arithmetic problems in the form of $a + b + c$ = ??, where a, b, and c were randomly selected integers ranging from 1 to 9. Mean accuracy across patients in the math task was 90.87% ± 7.22%, indicating that participants performed the math task with a high level of accuracy, similar to our previous studies (Das & Menon, 2022a). After a 20 sec post-encoding delay, participants were instructed to recall as many words as possible during the 30 sec recall period. Average recall accuracy across patients was 25.0% ± 10.6%, similar to prior studies of verbal episodic memory retrieval in neurosurgical patients (Burke et al., 2014). The mismatch in the number trials therefore made it difficult to directly compare causal signaling measures between successfully versus unsuccessfully recalled words. From the point of view of probing behaviorally effective memory encoding, our focus was therefore on successful recall for this and the subsequent tasks below, consistent with most prior studies (Long, Burke, & Kahana, 2014; Watrous, Tandon, Conner, Pieters, & Ekstrom, 2013). We analyzed iEEG epochs from the encoding and recall periods of the verbal free recall task. For the recall periods, iEEG recordings 1600 msec prior to the vocal onset of each word were analyzed (Solomon et al., 2019). Data from each trial was analyzed separately and specific measures were averaged across trials.

(b) Categorized verbal free recall (CATVFR) task

This task was very similar to the verbal free recall task. Here, patients performed multiple trials of a categorized free recall experiment, where they were presented with a list of words with consecutive pairs of words from a specific category (for example, JEANS-COAT, GRAPE-PEACH, etc.) and subsequently asked to recall as many as possible from the original list (**Figure**

1b) (Qasim et al., 2023). Similar to the uncategorized verbal free recall task, this task also consisted of three periods: encoding, delay, and recall. During encoding, a list of 12 words was visually presented for ~30 sec. Semantic categories were chosen using Amazon Mechanical Turk. Pairs of words from the same semantic category were never presented consecutively. Each word was presented for a duration of 1600 msec, followed by an inter-stimulus interval of 750 to 1000 msec. After a 20 sec post-encoding delay similar to the uncategorized verbal free recall task, participants were instructed to recall as many words as possible during the 30 sec recall period. Average accuracy across patients in the math task was 89.46% ± 9.90%. Average recall accuracy across patients was 29.6% ± 13.4%. Analysis of iEEG epochs from the encoding and recall periods of the categorized free recall task was same as the uncategorized verbal free recall task.

(c) Paired associates learning verbal cued recall (PALVCR) task

Patients performed multiple trials of a paired associates learning verbal cued recall experiment, where they were presented with a list of word-pairs and subsequently asked to recall based on the given word-cue (**Figure 1c**). Similar to the uncategorized verbal free recall task, this task also consisted of three periods: encoding, delay, and recall. During encoding, a list of 6 word-pairs was visually presented for ~36 sec. Similar to the uncategorized verbal free recall task, words were selected at random, without replacement, from a pool of high frequency English nouns (http://memory.psych.upenn.edu/Word_Pools). Each word was presented for a duration of 4000 msec, followed by an inter-stimulus interval of 1750 to 2000 msec. After a 20 sec post-encoding delay similar to the uncategorized verbal free recall task, participants were shown a specific word-cue for a duration of 4000 msec and asked to verbally recall the cued word from memory. Each word presentation during recall was followed by an inter-stimulus interval of 1750 to 2000 msec and the recall period lasted for ~36 sec. Average accuracy across patients in the math task was 93.91% ± 4.66%. Average recall accuracy across patients was 33.8% ± 25.9%. For encoding, iEEG recordings corresponding to the 4000 msec encoding period of the task were analyzed. For recall, iEEG recordings 1600 msec prior to the vocal onset of each word were analyzed (Solomon et al., 2019). Data from each trial was analyzed separately and specific measures were averaged across trials.

(d) Water maze spatial memory (WMSM) task

Patients performed multiple trials of a spatial memory experiment in a virtual navigation paradigm (Goyal et al., 2018; Jacobs et al., 2016; Lee et al., 2018) similar to the Morris water maze (Morris, 1984). The environment was rectangular (1.8:1 aspect ratio), and was surrounded by a continuous boundary (**Figure 1d**). There were four distal visual cues (landmarks), one centered on each side of the rectangle, to aid with orienting. Each trial (96 trials per session, 1–3 sessions per subject) started with two 5 sec encoding periods, during which subjects were driven to an object from a random starting location. At the beginning of an encoding period, the object appeared and, over the course of 5 sec, the subject was automatically driven directly toward it. The 5 sec period consisted of three intervals: first, the subject was rotated toward the object (1 sec), second, the subject was driven toward the object (3 sec), and, finally, the subject paused while at the object location (1 sec). After a 5 sec delay with a blank screen, the same process was repeated from a different starting location. After both encoding periods for each item, there was a

5 sec pause followed by the recall period. The subject was placed in the environment at a random starting location with the object hidden and then asked to freely navigate using a joystick to the location where they thought the object was located. When they reached their chosen location, they pressed a button to record their response. They then received feedback on their performance via an overhead view of the environment showing the actual and reported object locations. Average recall accuracy across patients was 48.1% ± 5.6%.

We analyzed the 5 sec iEEG epochs corresponding to the entire encoding and recall periods of the task as has been done previously (Goyal et al., 2018; Jacobs et al., 2016; Lee et al., 2018). Data from each trial was analyzed separately and specific measures were averaged across trials, similar to the verbal tasks.

Out of total 177 participants, 51% (91 out of 177) of participants participated in at least 2 experiments, 17% (30 out of 177) of participants participated in at least 3 experiments, and 6% (10 out of 177) of participants participated in all four experiments.

iEEG analysis of high-gamma power

We first filtered the signals in the high-gamma (80-160 Hz) frequency band (Canolty et al., 2006; Helfrich & Knight, 2016; Kai J. Miller, Weaver, & Ojemann, 2009) and then calculated the square of the filtered signals as the power of the signals (Kwon et al., 2021). Signals were then smoothed using 0.2s windows with 90% overlap (Kwon et al., 2021) and normalized with respect to 0.2s pre-stimulus periods.

iEEG analysis of phase transfer entropy (PTE) and causal dynamics

Phase transfer entropy (PTE) is a nonlinear measure of the directionality of information flow between time-series and can be applied as a measure of causality to nonstationary time-series (Das & Menon, 2021, 2022b; Lobier et al., 2014). Note that information flow described here relates to signaling between brain areas and does not necessarily reflect the representation or coding of behaviorally relevant variables per se. The PTE measure is in contrast to the Granger causality measure which can be applied only to stationary time-series (Barnett & Seth, 2014). We first carried out a stationarity test of the iEEG recordings (unit root test for stationarity (Barnett & Seth, 2014)) and found that the spectral radius of the autoregressive model is very close to one, indicating that the iEEG time-series is nonstationary. This precluded the applicability of the Granger causality analysis in our study.

Given two time-series $\{x_i\}$ and $\{y_i\}$, where $i = 1, 2, ..., M$, instantaneous phases were first extracted using the Hilbert transform. Let $\{x_i^p\}$ and $\{y_i^p\}$, where $i = 1, 2, ..., M$, denote the corresponding phase time-series. If the uncertainty of the target signal $\{y_i^p\}$ at delay τ is quantified using Shannon entropy, then the PTE from driver signal $\{x_i^p\}$ to target signal $\{y_i^p\}$ can be given by

$$PTE_{x \to y} = \sum_i p\left(y_{i+\tau}^p, y_i^p, x_i^p\right) \log\left(\frac{p\left(y_{i+\tau}^p \mid y_i^p, x_i^p\right)}{p\left(y_{i+\tau}^p \mid y_i^p\right)}\right), \quad \text{(i)}$$

where the probabilities can be calculated by building histograms of occurrences of singles, pairs, or triplets of instantaneous phase estimates from the phase time-series (Hillebrand et al., 2016). For our analysis, the number of bins in the histograms was set as $3.49 \times STD \times M^{-1/3}$ and delay τ was set as $2M/M_{\pm}$, where STD is average standard deviation of the phase time-series $\{x_i^p\}$ and $\{y_i^p\}$ and $M_{\pm}$ is the number of times the phase changes sign across time and channels (Hillebrand et al., 2016). PTE has been shown to be robust against the choice of the delay τ and the number of bins for forming the histograms (Hillebrand et al., 2016). In our analysis, PTE was calculated for the entire encoding and recall periods for each trial and then averaged across trials.

Net causal outflow was calculated as the difference between the total outgoing information and total incoming information, that is, net causal outflow = PTE(out) − PTE(in). For example, for calculation of PTE(out) and PTE(in) for the AI electrodes, electrodes in the PCC/precuneus, mPFC, dPPC, and MFG were considered, that is, PTE(out) was calculated as the net PTE from AI electrodes to the PCC/precuneus, mPFC, dPPC, and MFG electrodes, and PTE(in) was calculated as the net PTE from the PCC/precuneus, mPFC, dPPC, and MFG electrodes to AI electrodes. Net causal outflow for the PCC/precuneus, mPFC, dPPC, and MFG electrodes were calculated similarly.

Statistical analysis

Statistical analysis was conducted using mixed effects analysis with the lmerTest package (Kuznetsova, Brockhoff, & Christensen, 2017) implemented in R software (version 4.0.2, R Foundation for Statistical Computing). Because PTE data were not normally distributed, we used BestNormalize (Peterson & Cavanaugh, 2018) which contains a suite of transformation-estimating functions that can be used to optimally normalize data. The resulting normally distributed data were subjected to mixed effects analysis with the following model: *PTE ~ Condition + (1|Subject)*, where *Condition* models the fixed effects (condition differences) and (1|*Subject*) models the random repeated measurements within the same participant. Analysis of variance (ANOVA) was used to test the significance of findings with FDR-corrections for multiple comparisons ($p<0.05$). Similar mixed effects statistical analysis procedures were used for comparison of high-gamma power across task conditions, where the mixed effects analysis was run on each of the 0.2s windows.

For effect size estimation, we used Cohen's *d* statistics for pairwise comparisons. We used the *lme.dscore()* function in the *EMAtools* package in R for estimating Cohen's *d*.

Bayesian replication analysis

We used replication Bayes factor (Ly et al., 2019; Verhagen & Wagenmakers, 2014) analysis to estimate the degree of replicability for the direction of information flow for each frequency and task condition and across task domains. Analysis was implemented in R software using the BayesFactor package (Rouder, Speckman, Sun, Morey, & Iverson, 2009). Because PTE data were not normally distributed, as previously, we used BestNormalize (Peterson & Cavanaugh, 2018) to optimally normalize data. We calculated the replication Bayes factor for pairwise experiments. We compared the Bayes factor of the joint model *PTE(task1+task2) ~ Condition + (1|Subject)* with the Bayes factor (BF) of individual model as *PTE(task1) ~ Condition +*

(1|Subject), where *task1* denotes the verbal free recall (original) task and *task2* denotes the categorized verbal free recall, paired associates learning verbal cued recall, or water maze spatial memory (replication) conditions. We calculated the ratio *BF(task1+task2)/BF(task1)*, which was used to quantify the degree of replicability. We determined whether the degree of replicability was higher than 3 as Bayes factor of at least 3 indicates evidence for replicability (Jeffreys, 1998). A Bayes factor of at least 100 is considered as "*decisive*" for degree of replication (Jeffreys, 1998). Same analysis procedures were used to estimate the degree of replicability for high-gamma power comparison of DMN and FPN electrodes with the AI electrodes, across experiments.

References

Andermane, N., Joensen, B. H., & Horner, A. J. (2021). Forgetting across a hierarchy of episodic representations. *Curr Opin Neurobiol, 67*, 50-57. doi:10.1016/j.conb.2020.08.004

Andrews-Hanna, J. R. (2012). The brain's default network and its adaptive role in internal mentation. *Neuroscientist, 18*(3), 251-270. doi:10.1177/1073858411403316

Atkinson, R. C., & Shiffrin, R. M. (1968). Human memory: a proposed system and its control processes. *Psychology of Learning and Motivation, 2*, 89-195.

Badre, D., Poldrack, R. A., Paré-Blagoev, E. J., Insler, R. Z., & Wagner, A. D. (2005). Dissociable controlled retrieval and generalized selection mechanisms in ventrolateral prefrontal cortex. *Neuron, 47*(6), 907-918. doi:10.1016/j.neuron.2005.07.023

Badre, D., & Wagner, A. D. (2007). Left ventrolateral prefrontal cortex and the cognitive control of memory. *Neuropsychologia, 45*(13), 2883-2901. doi:10.1016/j.neuropsychologia.2007.06.015

Barnett, L., & Seth, A. K. (2014). The MVGC multivariate Granger causality toolbox: A new approach to Granger-causal inference. *Journal of Neuroscience Methods, 223*, 50-68. doi:10.1016/j.jneumeth.2013.10.018

Bassett, D. S., & Sporns, O. (2017). Network neuroscience. *Nat Neurosci, 20*(3), 353-364. doi:10.1038/nn.4502

Bastos, A. M., Usrey, W. M., Adams, R. A., Mangun, G. R., Fries, P., & Friston, K. J. (2012). Canonical microcircuits for predictive coding. *Neuron, 76*(4), 695-711. doi:10.1016/j.neuron.2012.10.038

Bastos, A. M., Vezoli, J., Bosman, C. A., Schoffelen, J. M., Oostenveld, R., Dowdall, J. R., . . . Fries, P. (2015). Visual areas exert feedforward and feedback influences through distinct frequency channels. *Neuron, 85*(2), 390-401. doi:10.1016/j.neuron.2014.12.018

Bonthius, D. J., Solodkin, A., & Van Hoesen, G. W. (2005). Pathology of the insular cortex in Alzheimer disease depends on cortical architecture. *J Neuropathol Exp Neurol, 64*(10), 910-922. doi:10.1097/01.jnen.0000182983.87106.d1

Bressler, S. L., & Menon, V. (2010). Large-scale brain networks in cognition: emerging methods and principles. *Trends in Cognitive Sciences, 14*(6), 277-290. doi:10.1016/j.tics.2010.04.004

Buckner, R. L., Andrews-Hanna, J. R., & Schacter, D. L. (2008). The brain's default network: anatomy, function, and relevance to disease. *Ann N Y Acad Sci, 1124*, 1-38. doi:10.1196/annals.1440.011

Burke, J. F., Sharan, A. D., Sperling, M. R., Ramayya, A. G., Evans, J. J., Healey, M. K., . . . Kahana, M. J. (2014). Theta and high-frequency activity mark spontaneous recall of episodic memories. *J Neurosci, 34*(34), 11355-11365. doi:10.1523/jneurosci.2654-13.2014

Burke, J. F., Zaghloul, K. A., Jacobs, J., Williams, R. B., Sperling, M. R., Sharan, A. D., & Kahana, M. J. (2013). Synchronous and asynchronous theta and gamma activity during episodic memory formation. *J Neurosci, 33*(1), 292-304. doi:10.1523/jneurosci.2057-12.2013

Cai, W., Chen, T., Ryali, S., Kochalka, J., Li, C. S., & Menon, V. (2016). Causal Interactions Within a Frontal-Cingulate-Parietal Network During Cognitive Control: Convergent Evidence from a Multisite-Multitask Investigation. *Cereb Cortex, 26*(5), 2140-2153. doi:10.1093/cercor/bhv046

Cai, W., Ryali, S., Chen, T., Li, C. S., & Menon, V. (2014). Dissociable roles of right inferior frontal cortex and anterior insula in inhibitory control: evidence from intrinsic and task-related functional parcellation, connectivity, and response profile analyses across multiple datasets. *J Neurosci, 34*(44), 14652-14667. doi:10.1523/jneurosci.3048-14.2014

Cai, W., Ryali, S., Pasumarthy, R., Talasila, V., & Menon, V. (2021). Dynamic causal brain circuits during working memory and their functional controllability. *Nat Commun, 12*(1), 3314. doi:10.1038/s41467-021-23509-x

Canolty, R. T., Edwards, E., Dalal, S. S., Soltani, M., Nagarajan, S. S., Kirsch, H. E., . . . Knight, R. T. (2006). High gamma power is phase-locked to theta oscillations in human neocortex. *Science, 313*(5793), 1626-1628. doi:10.1126/science.1128115

Canolty, R. T., & Knight, R. T. (2010). The functional role of cross-frequency coupling. *Trends Cogn Sci, 14*(11), 506-515. doi:10.1016/j.tics.2010.09.001

Chen, T., Cai, W., Ryali, S., Supekar, K., & Menon, V. (2016). Distinct Global Brain Dynamics and Spatiotemporal Organization of the Salience Network. *PLOS Biology, 14*(6), e1002469. doi:10.1371/journal.pbio.1002469

Crone, N. E., Boatman, D., Gordon, B., & Hao, L. (2001). Induced electrocorticographic gamma activity during auditory perception. Brazier Award-winning article, 2001. *Clin Neurophysiol, 112*(4), 565-582. doi:10.1016/s1388-2457(00)00545-9

Daitch, A. L., & Parvizi, J. (2018). Spatial and temporal heterogeneity of neural responses in human posteromedial cortex. *Proc Natl Acad Sci U S A, 115*(18), 4785-4790. doi:10.1073/pnas.1721714115

Das, A., de Los Angeles, C., & Menon, V. (2022). Electrophysiological foundations of the human default-mode network revealed by intracranial-EEG recordings during resting-state and cognition. *Neuroimage, 250*, 118927. doi:10.1016/j.neuroimage.2022.118927

Das, A., & Menon, V. (2020). Spatiotemporal Integrity and Spontaneous Nonlinear Dynamic Properties of the Salience Network Revealed by Human Intracranial Electrophysiology: A Multicohort Replication. *Cereb Cortex, 30*(10), 5309-5321. doi:10.1093/cercor/bhaa111

Das, A., & Menon, V. (2021). Asymmetric Frequency-Specific Feedforward and Feedback Information Flow between Hippocampus and Prefrontal Cortex during Verbal Memory Encoding and Recall. *J Neurosci, 41*(40), 8427-8440. doi:10.1523/jneurosci.0802-21.2021

Das, A., & Menon, V. (2022a). Causal dynamics and information flow in parietal-temporal-hippocampal circuits during mental arithmetic revealed by high-temporal resolution human intracranial EEG. *Cortex, 147*, 24-40. doi:10.1016/j.cortex.2021.11.012

Das, A., & Menon, V. (2022b). Replicable patterns of causal information flow between hippocampus and prefrontal cortex during spatial navigation and spatial-verbal memory formation. *Cereb Cortex, 32*(23), 5343-5361. doi:10.1093/cercor/bhac018

Das, A., & Menon, V. (2023). Concurrent- and after-effects of medial temporal lobe stimulation on directed information flow to and from prefrontal and parietal cortices during memory formation. *J Neurosci, 43*(17), 3159-3175. doi:10.1523/jneurosci.1728-22.2023

Das, A., Myers, J., Mathura, R., Shofty, B., Metzger, B. A., Bijanki, K., . . . Sheth, S. A. (2022). Spontaneous neuronal oscillations in the human insula are hierarchically organized traveling waves. *Elife, 11*. doi:10.7554/eLife.76702

Davis, Z. W., Muller, L., Martinez-Trujillo, J., Sejnowski, T., & Reynolds, J. H. (2020). Spontaneous travelling cortical waves gate perception in behaving primates. *Nature, 587*(7834), 432-436. doi:10.1038/s41586-020-2802-y

Davis, Z. W., Muller, L., & Reynolds, J. H. (2022). Spontaneous Spiking Is Governed by Broadband Fluctuations. *J Neurosci, 42*(26), 5159-5172. doi:10.1523/jneurosci.1899-21.2022

Dickerson, B. C., & Eichenbaum, H. (2010). The episodic memory system: neurocircuitry and disorders. *Neuropsychopharmacology, 35*(1), 86-104. doi:10.1038/npp.2009.126

Dosenbach, N. U., Fair, D. A., Cohen, A. L., Schlaggar, B. L., & Petersen, S. E. (2008). A dual-networks architecture of top-down control. *Trends Cogn Sci, 12*(3), 99-105. doi:10.1016/j.tics.2008.01.001

Dosenbach, N. U., Visscher, K. M., Palmer, E. D., Miezin, F. M., Wenger, K. K., Kang, H. C., . . . Petersen, S. E. (2006). A core system for the implementation of task sets. *Neuron, 50*(5), 799-812. doi:10.1016/j.neuron.2006.04.031

Düzel, E., Penny, W. D., & Burgess, N. (2010). Brain oscillations and memory. *Curr Opin Neurobiol, 20*(2), 143-149. doi:10.1016/j.conb.2010.01.004

Edwards, E., Soltani, M., Deouell, L. Y., Berger, M. S., & Knight, R. T. (2005). High gamma activity in response to deviant auditory stimuli recorded directly from human cortex. *J Neurophysiol, 94*(6), 4269-4280. doi:10.1152/jn.00324.2005

Ezzyat, Y., Wanda, P. A., Levy, D. F., Kadel, A., Aka, A., Pedisich, I., . . . Kahana, M. J. (2018). Closed-loop stimulation of temporal cortex rescues functional networks and improves memory. *Nat Commun, 9*(1), 365. doi:10.1038/s41467-017-02753-0

Faillenot, I., Heckemann, R. A., Frot, M., & Hammers, A. (2017). Macroanatomy and 3D probabilistic atlas of the human insula. *Neuroimage, 150*, 88-98. doi:10.1016/j.neuroimage.2017.01.073

Fan, L., Li, H., Zhuo, J., Zhang, Y., Wang, J., Chen, L., . . . Jiang, T. (2016). The Human Brainnetome Atlas: A New Brain Atlas Based on Connectional Architecture. *Cereb Cortex, 26*(8), 3508-3526. doi:10.1093/cercor/bhw157

Fox, M. D., & Raichle, M. E. (2007). Spontaneous fluctuations in brain activity observed with functional magnetic resonance imaging. *Nat Rev Neurosci, 8*(9), 700-711. doi:10.1038/nrn2201

Fox, M. D., Snyder, A. Z., Vincent, J. L., Corbetta, M., Van Essen, D. C., & Raichle, M. E. (2005). The human brain is intrinsically organized into dynamic, anticorrelated functional networks. *Proc Natl Acad Sci U S A, 102*(27), 9673-9678. doi:10.1073/pnas.0504136102

Frauscher, B., von Ellenrieder, N., Zelmann, R., Doležalová, I., Minotti, L., Olivier, A., . . . Gotman, J. (2018). Atlas of the normal intracranial electroencephalogram: neurophysiological awake activity in different cortical areas. *Brain, 141*(4), 1130-1144. doi:10.1093/brain/awy035

Golby, A. J., Poldrack, R. A., Brewer, J. B., Spencer, D., Desmond, J. E., Aron, A. P., & Gabrieli, J. D. (2001). Material-specific lateralization in the medial temporal lobe and prefrontal cortex during memory encoding. *Brain, 124*(Pt 9), 1841-1854. doi:10.1093/brain/124.9.1841

Goyal, A., Miller, J., Watrous, A. J., Lee, S. A., Coffey, T., Sperling, M. R., . . . Jacobs, J. (2018). Electrical Stimulation in Hippocampus and Entorhinal Cortex Impairs Spatial and Temporal Memory. *J Neurosci, 38*(19), 4471-4481. doi:10.1523/jneurosci.3049-17.2018

Grady, C. L., Furey, M. L., Pietrini, P., Horwitz, B., & Rapoport, S. I. (2001). Altered brain functional connectivity and impaired short-term memory in Alzheimer's disease. *Brain, 124*(Pt 4), 739-756. doi:10.1093/brain/124.4.739

Greicius, M. D., Kiviniemi, V., Tervonen, O., Vainionpää, V., Alahuhta, S., Reiss, A. L., & Menon, V. (2008). Persistent default-mode network connectivity during light sedation. *Human Brain Mapping, 29*(7), 839-847. doi:10.1002/hbm.20537

Greicius, M. D., & Menon, V. (2004). Default-Mode Activity during a Passive Sensory Task: Uncoupled from Deactivation but Impacting Activation. *Journal of Cognitive Neuroscience, 16*(9), 1484-1492. doi:10.1162/0898929042568532

Grover, S., Nguyen, J. A., & Reinhart, R. M. G. (2021). Synchronizing Brain Rhythms to Improve Cognition. *Annu Rev Med, 72*, 29-43. doi:10.1146/annurev-med-060619-022857

Guzmán-Vélez, E., Diez, I., Schoemaker, D., Pardilla-Delgado, E., Vila-Castelar, C., Fox-Fuller, J. T., . . . Quiroz, Y. T. (2022). Amyloid-β and tau pathologies relate to distinctive brain dysconnectomics in preclinical autosomal-dominant Alzheimer's disease. *Proc Natl Acad Sci U S A, 119*(15), e2113641119. doi:10.1073/pnas.2113641119

Helfrich, R. F., & Knight, R. T. (2016). Oscillatory Dynamics of Prefrontal Cognitive Control. *Trends Cogn Sci, 20*(12), 916-930. doi:10.1016/j.tics.2016.09.007

Hermes, D., Nguyen, M., & Winawer, J. (2017). Neuronal synchrony and the relation between the blood-oxygen-level dependent response and the local field potential. *PLoS Biol, 15*(7), e2001461. doi:10.1371/journal.pbio.2001461

Hillebrand, A., Tewarie, P., van Dellen, E., Yu, M., Carbo, E. W., Douw, L., . . . Stam, C. J. (2016). Direction of information flow in large-scale resting-state networks is frequency-dependent. *Proc Natl Acad Sci U S A, 113*(14), 3867-3872. doi:10.1073/pnas.1515657113

Huang, Y., & Keller, C. (2022). How can I investigate causal brain networks with iEEG? In N. Axmacher (Ed.), *Intracranial EEG for Cognitive Neuroscientists*: Springer.

Hutchison, R. M., Hashemi, N., Gati, J. S., Menon, R. S., & Everling, S. (2015). Electrophysiological signatures of spontaneous BOLD fluctuations in macaque prefrontal cortex. *Neuroimage, 113*, 257-267. doi:10.1016/j.neuroimage.2015.03.062

Jacobs, J., Miller, J., Lee, S. A., Coffey, T., Watrous, A. J., Sperling, M. R., . . . Rizzuto, D. S. (2016). Direct Electrical Stimulation of the Human Entorhinal Region and Hippocampus Impairs Memory. *Neuron, 92*(5), 983-990. doi:10.1016/j.neuron.2016.10.062

Jeffreys, H. (1998). *The Theory of Probability* (3rd ed.). Oxford, England: Oxford University Press.

Jin, Y., Olk, B., & Hilgetag, C. C. (2010). Contributions of human parietal and frontal cortices to attentional control during conflict resolution: a 1-Hz offline rTMS study. *Exp Brain Res, 205*(1), 131-138. doi:10.1007/s00221-010-2336-x

Kelley, W. M., Miezin, F. M., McDermott, K. B., Buckner, R. L., Raichle, M. E., Cohen, N. J., . . . Petersen, S. E. (1998). Hemispheric specialization in human dorsal frontal cortex and medial temporal lobe for verbal and nonverbal memory encoding. *Neuron, 20*(5), 927-936. doi:10.1016/s0896-6273(00)80474-2

Kronemer, S. I., Aksen, M., Ding, J. Z., Ryu, J. H., Xin, Q., Ding, Z., . . . Blumenfeld, H. (2022). Human visual consciousness involves large scale cortical and subcortical networks independent of task report and eye movement activity. *Nat Commun, 13*(1), 7342. doi:10.1038/s41467-022-35117-4

Kucyi, A., Daitch, A., Raccah, O., Zhao, B., Zhang, C., Esterman, M., . . . Parvizi, J. (2020). Electrophysiological dynamics of antagonistic brain networks reflect attentional fluctuations. *Nat Commun, 11*(1), 325. doi:10.1038/s41467-019-14166-2

Kumaran, D., & McClelland, J. L. (2012). Generalization through the recurrent interaction of episodic memories: a model of the hippocampal system. *Psychol Rev, 119*(3), 573-616. doi:10.1037/a0028681

Kuznetsova, A., Brockhoff, P. B., & Christensen, R. H. B. (2017). lmerTest Package: Tests in Linear Mixed Effects Models. *Journal of Statistical Software, 82*(13), 1-26.

Kwon, H., Kronemer, S. I., Christison-Lagay, K. L., Khalaf, A., Li, J., Ding, J. Z., . . . Blumenfeld, H. (2021). Early cortical signals in visual stimulus detection. *Neuroimage, 244*, 118608. doi:10.1016/j.neuroimage.2021.118608

Lachaux, J. P., George, N., Tallon-Baudry, C., Martinerie, J., Hugueville, L., Minotti, L., . . . Renault, B. (2005). The many faces of the gamma band response to complex visual stimuli. *Neuroimage, 25*(2), 491-501. doi:10.1016/j.neuroimage.2004.11.052

Lakatos, P., Gross, J., & Thut, G. (2019). A New Unifying Account of the Roles of Neuronal Entrainment. *Curr Biol, 29*(18), R890-r905. doi:10.1016/j.cub.2019.07.075

Laufs, H., Krakow, K., Sterzer, P., Eger, E., Beyerle, A., Salek-Haddadi, A., & Kleinschmidt, A. (2003). Electroencephalographic signatures of attentional and cognitive default modes in spontaneous brain activity fluctuations at rest. *Proc Natl Acad Sci U S A, 100*(19), 11053-11058. doi:10.1073/pnas.1831638100

Lee, S. A., Miller, J. F., Watrous, A. J., Sperling, M. R., Sharan, A., Worrell, G. A., . . . Jacobs, J. (2018). Electrophysiological Signatures of Spatial Boundaries in the Human Subiculum. *J Neurosci, 38*(13), 3265-3272. doi:10.1523/jneurosci.3216-17.2018

Leopold, D. A., Murayama, Y., & Logothetis, N. K. (2003). Very Slow Activity Fluctuations in Monkey Visual Cortex: Implications for Functional Brain Imaging. *Cerebral Cortex, 13*(4), 422-433. doi:10.1093/cercor/13.4.422

Llorens, A., Bellier, L., Blenkmann, A. O., Ivanovic, J., Larsson, P. G., Lin, J. J., . . . Knight, R. T. (2023). Decision and response monitoring during working memory are sequentially represented in the human insula. *iScience, 26*(10), 107653. doi:10.1016/j.isci.2023.107653

Lobier, M., Siebenhühner, F., Palva, S., & Matias, P. J. (2014). Phase transfer entropy: A novel phase-based measure for directed connectivity in networks coupled by oscillatory interactions. *Neuroimage, 85*, 853-872. doi:10.1016/j.neuroimage.2013.08.056

Long, N. M., Burke, J. F., & Kahana, M. J. (2014). Subsequent memory effect in intracranial and scalp EEG. *Neuroimage, 84*, 488-494. doi:10.1016/j.neuroimage.2013.08.052

Ly, A., Etz, A., Marsman, M., & Wagenmakers, E. J. (2019). Replication Bayes factors from evidence updating. *Behav Res Methods, 51*(6), 2498-2508. doi:10.3758/s13428-018-1092-x

Mainy, N., Kahane, P., Minotti, L., Hoffmann, D., Bertrand, O., & Lachaux, J. P. (2007). Neural correlates of consolidation in working memory. *Hum Brain Mapp, 28*(3), 183-193. doi:10.1002/hbm.20264

Mantini, D., Perrucci, M. G., Del Gratta, C., Romani, G. L., & Corbetta, M. (2007). Electrophysiological signatures of resting state networks in the human brain. *Proc Natl Acad Sci U S A, 104*(32), 13170-13175. doi:10.1073/pnas.0700668104

Menon, V. (2011). Large-scale brain networks and psychopathology: a unifying triple network model. *Trends Cogn Sci, 15*(10), 483-506. doi:10.1016/j.tics.2011.08.003

Menon, V. (2015). Salience Network. In A. W. Toga (Ed.), *Brain Mapping* (pp. 597-611). Waltham: Academic Press.
Menon, V. (2023). 20 years of the default mode network: a review and synthesis. *Neuron*.
Menon, V., Freeman, W. J., Cutillo, B. A., Desmond, J. E., Ward, M. F., Bressler, S. L., . . . Gevins, A. S. (1996). Spatio-temporal correlations in human gamma band electrocorticograms. *Electroencephalography and Clinical Neurophysiology, 98*(2), 89-102. doi:10.1016/0013-4694(95)00206-5
Menon, V., & Uddin, L. Q. (2010). Saliency, switching, attention and control: a network model of insula function. *Brain Structure and Function, 214*(5), 655-667. doi:10.1007/s00429-010-0262-0
Mercier, M. R., Dubarry, A. S., Tadel, F., Avanzini, P., Axmacher, N., Cellier, D., . . . Oostenveld, R. (2022). Advances in human intracranial electroencephalography research, guidelines and good practices. *Neuroimage*, 119438. doi:10.1016/j.neuroimage.2022.119438
Mesulam, M. M. (1990). Large-scale neurocognitive networks and distributed processing for attention, language, and memory. *Ann Neurol, 28*(5), 597-613. doi:10.1002/ana.410280502
Miller, K. J., Leuthardt, E. C., Schalk, G., Rao, R. P., Anderson, N. R., Moran, D. W., . . . Ojemann, J. G. (2007). Spectral changes in cortical surface potentials during motor movement. *J Neurosci, 27*(9), 2424-2432. doi:10.1523/jneurosci.3886-06.2007
Miller, K. J., Weaver, K. E., & Ojemann, J. G. (2009). Direct electrophysiological measurement of human default network areas. *Proceedings of the National Academy of Sciences, 106*(29), 12174-12177. doi:10.1073/pnas.0902071106
Morris, R. (1984). Developments of a water-maze procedure for studying spatial learning in the rat. *J Neurosci Methods, 11*(1), 47-60. doi:10.1016/0165-0270(84)90007-4
Moscovitch, M., Cabeza, R., Winocur, G., & Nadel, L. (2016). Episodic Memory and Beyond: The Hippocampus and Neocortex in Transformation. *Annu Rev Psychol, 67*, 105-134. doi:10.1146/annurev-psych-113011-143733
Nagel, B. J., Herting, M. M., Maxwell, E. C., Bruno, R., & Fair, D. (2013). Hemispheric lateralization of verbal and spatial working memory during adolescence. *Brain Cogn, 82*(1), 58-68. doi:10.1016/j.bandc.2013.02.007
Peterson, R. A., & Cavanaugh, J. E. (2018). Ordered quantile normalization: a semiparametric transformation built for the cross-validation era. *Journal of Applied Statistics, 82*(13-15), 2312–2327.
Qasim, S. E., Mohan, U. R., Stein, J. M., & Jacobs, J. (2023). Neuronal activity in the human amygdala and hippocampus enhances emotional memory encoding. *Nat Hum Behav*. doi:10.1038/s41562-022-01502-8
Raichle, M. E. (2015). The brain's default mode network. *Annu Rev Neurosci, 38*, 433-447. doi:10.1146/annurev-neuro-071013-014030
Raichle, M. E., MacLeod, A. M., Snyder, A. Z., Powers, W. J., Gusnard, D. A., & Shulman, G. L. (2001). A default mode of brain function. *Proc Natl Acad Sci U S A, 98*(2), 676-682. doi:10.1073/pnas.98.2.676
Ranganath, C., & Ritchey, M. (2012). Two cortical systems for memory-guided behaviour. *Nat Rev Neurosci, 13*(10), 713-726. doi:10.1038/nrn3338
Ray, S., Crone, N. E., Niebur, E., Franaszczuk, P. J., & Hsiao, S. S. (2008). Neural correlates of high-gamma oscillations (60-200 Hz) in macaque local field potentials and their potential

implications in electrocorticography. *J Neurosci, 28*(45), 11526-11536. doi:10.1523/jneurosci.2848-08.2008
Rouder, J. N., Speckman, P. L., Sun, D., Morey, R. D., & Iverson, G. (2009). Bayesian t tests for accepting and rejecting the null hypothesis. *Psychon Bull Rev, 16*(2), 225-237. doi:10.3758/pbr.16.2.225
Rugg, M. D., & Vilberg, K. L. (2013). Brain networks underlying episodic memory retrieval. *Curr Opin Neurobiol, 23*(2), 255-260. doi:10.1016/j.conb.2012.11.005
Rutishauser, U., Reddy, L., Mormann, F., & Sarnthein, J. (2021). The Architecture of Human Memory: Insights from Human Single-Neuron Recordings. *J Neurosci, 41*(5), 883-890. doi:10.1523/jneurosci.1648-20.2020
Schölvinck, M. L., Maier, A., Ye, F. Q., Duyn, J. H., & Leopold, D. A. (2010). Neural basis of global resting-state fMRI activity. *Proceedings of the National Academy of Sciences, 107*(22), 10238-10243. doi:10.1073/pnas.0913110107
Sederberg, P. B., Schulze-Bonhage, A., Madsen, J. R., Bromfield, E. B., Litt, B., Brandt, A., & Kahana, M. J. (2007). Gamma oscillations distinguish true from false memories. *Psychol Sci, 18*(11), 927-932. doi:10.1111/j.1467-9280.2007.02003.x
Seeley, W. W., Menon, V., Schatzberg, A. F., Keller, J., Glover, G. H., Kenna, H., . . . Greicius, M. D. (2007). Dissociable Intrinsic Connectivity Networks for Salience Processing and Executive Control. *Journal of Neuroscience, 27*(9), 2349-2356. doi:10.1523/JNEUROSCI.5587-06.2007
Shine, J. M., Kucyi, A., Foster, B. L., Bickel, S., Wang, D., Liu, H., . . . Parvizi, J. (2017). Distinct Patterns of Temporal and Directional Connectivity among Intrinsic Networks in the Human Brain. *Journal of Neuroscience, 37*(40), 9667-9674. doi:10.1523/JNEUROSCI.1574-17.2017
Simons, J. S., & Spiers, H. J. (2003). Prefrontal and medial temporal lobe interactions in long-term memory. *Nat Rev Neurosci, 4*(8), 637-648. doi:10.1038/nrn1178
Smallwood, J., Bernhardt, B. C., Leech, R., Bzdok, D., Jefferies, E., & Margulies, D. S. (2021). The default mode network in cognition: a topographical perspective. *Nat Rev Neurosci, 22*(8), 503-513. doi:10.1038/s41583-021-00474-4
Solomon, E. A., Kragel, J. E., Sperling, M. R., Sharan, A., Worrell, G., Kucewicz, M., . . . Kahana, M. J. (2017). Widespread theta synchrony and high-frequency desynchronization underlies enhanced cognition. *Nature Communications, 8*(1), 1704. doi:10.1038/s41467-017-01763-2
Solomon, E. A., Stein, J. M., Das, S., Gorniak, R., Sperling, M. R., Worrell, G., . . . Kahana, M. J. (2019). Dynamic Theta Networks in the Human Medial Temporal Lobe Support Episodic Memory. *Curr Biol, 29*(7), 1100-1111.e1104. doi:10.1016/j.cub.2019.02.020
Sridharan, D., Levitin, D. J., & Menon, V. (2008). A critical role for the right fronto-insular cortex in switching between central-executive and default-mode networks. *Proceedings of the National Academy of Sciences, 105*(34), 12569-12574. doi:10.1073/pnas.0800005105
Tallon-Baudry, C., Bertrand, O., Hénaff, M. A., Isnard, J., & Fischer, C. (2005). Attention modulates gamma-band oscillations differently in the human lateral occipital cortex and fusiform gyrus. *Cereb Cortex, 15*(5), 654-662. doi:10.1093/cercor/bhh167
Thomason, M. E., Race, E., Burrows, B., Whitfield-Gabrieli, S., Glover, G. H., & Gabrieli, J. D. (2009). Development of spatial and verbal working memory capacity in the human brain. *J Cogn Neurosci, 21*(2), 316-332. doi:10.1162/jocn.2008.21028

Tulving, E. (2002). Episodic memory: from mind to brain. *Annu Rev Psychol, 53*, 1-25. doi:10.1146/annurev.psych.53.100901.135114

Uddin, L. Q. (2015). Salience processing and insular cortical function and dysfunction. *Nat Rev Neurosci, 16*(1), 55-61. doi:10.1038/nrn3857

Uhlhaas, P. J., & Singer, W. (2006). Neural synchrony in brain disorders: relevance for cognitive dysfunctions and pathophysiology. *Neuron, 52*(1), 155-168. doi:10.1016/j.neuron.2006.09.020

Uncapher, M. R., & Wagner, A. D. (2009). Posterior parietal cortex and episodic encoding: insights from fMRI subsequent memory effects and dual-attention theory. *Neurobiol Learn Mem, 91*(2), 139-154. doi:10.1016/j.nlm.2008.10.011

Verhagen, J., & Wagenmakers, E. J. (2014). Bayesian tests to quantify the result of a replication attempt. *J Exp Psychol Gen, 143*(4), 1457-1475. doi:10.1037/a0036731

Wagner, A. D., Paré-Blagoev, E. J., Clark, J., & Poldrack, R. A. (2001). Recovering meaning: left prefrontal cortex guides controlled semantic retrieval. *Neuron, 31*(2), 329-338. doi:10.1016/s0896-6273(01)00359-2

Wagner, A. D., Shannon, B. J., Kahn, I., & Buckner, R. L. (2005). Parietal lobe contributions to episodic memory retrieval. *Trends Cogn Sci, 9*(9), 445-453. doi:10.1016/j.tics.2005.07.001

Wang, M. Y., Wang, J., Zhou, J., Guan, Y. G., Zhai, F., Liu, C. Q., . . . Luan, G. M. (2017). Identification of the epileptogenic zone of temporal lobe epilepsy from stereo-electroencephalography signals: A phase transfer entropy and graph theory approach. *Neuroimage Clin, 16*, 184-195. doi:10.1016/j.nicl.2017.07.022

Watrous, A. J., Tandon, N., Conner, C. R., Pieters, T., & Ekstrom, A. D. (2013). Frequency-specific network connectivity increases underlie accurate spatiotemporal memory retrieval. *Nature Neuroscience, 16*(3), 349-356. doi:10.1038/nn.3315

Wen, X., Liu, Y., Yao, L., & Ding, M. (2013). Top-down regulation of default mode activity in spatial visual attention. *J Neurosci, 33*(15), 6444-6453. doi:10.1523/jneurosci.4939-12.2013

Yonelinas, A. P., Ranganath, C., Ekstrom, A. D., & Wiltgen, B. J. (2019). A contextual binding theory of episodic memory: systems consolidation reconsidered. *Nat Rev Neurosci, 20*(6), 364-375. doi:10.1038/s41583-019-0150-4

Figures

Figure 1.

(a) Experiment 1 — VFR

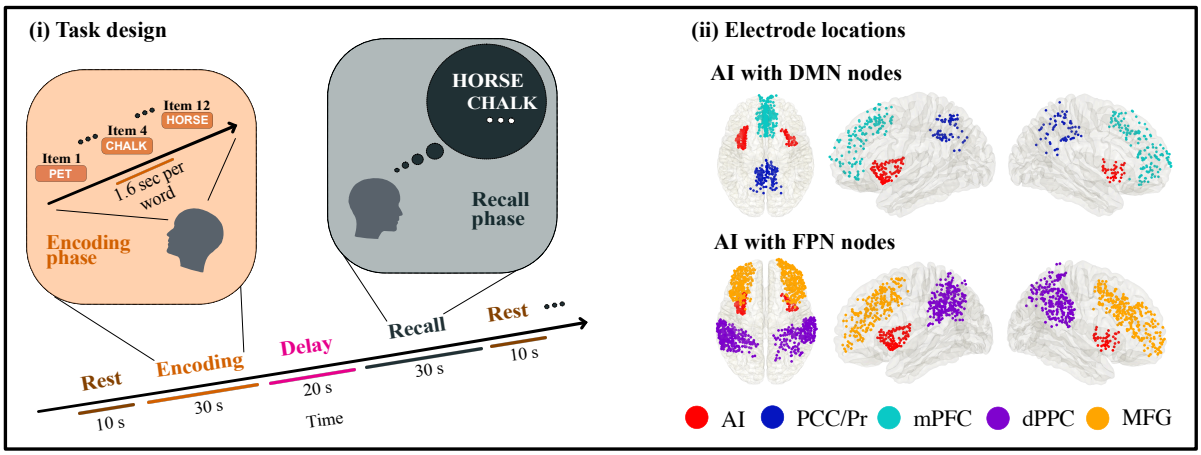

(b) Experiment 2 — CATVFR

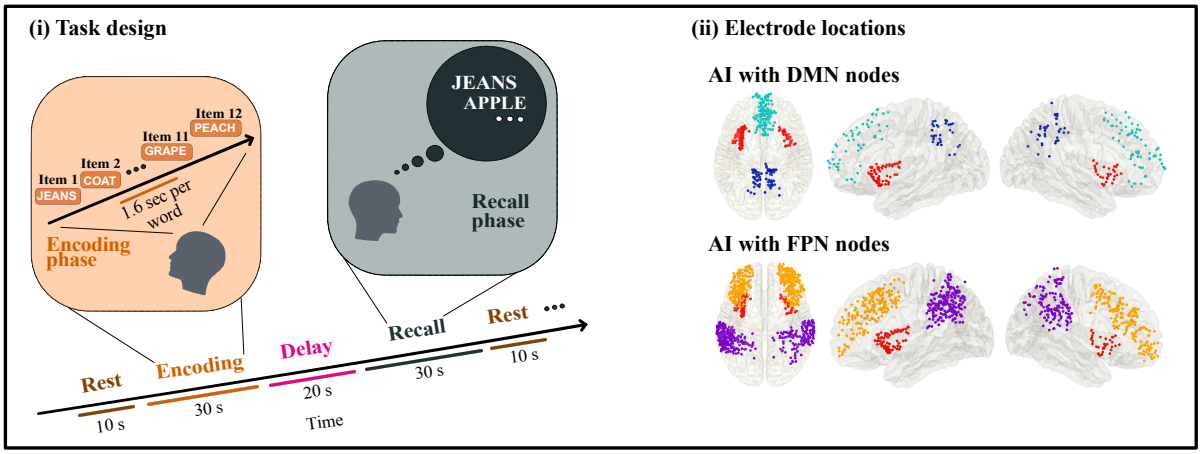

(c) Experiment 3 — PALVCR

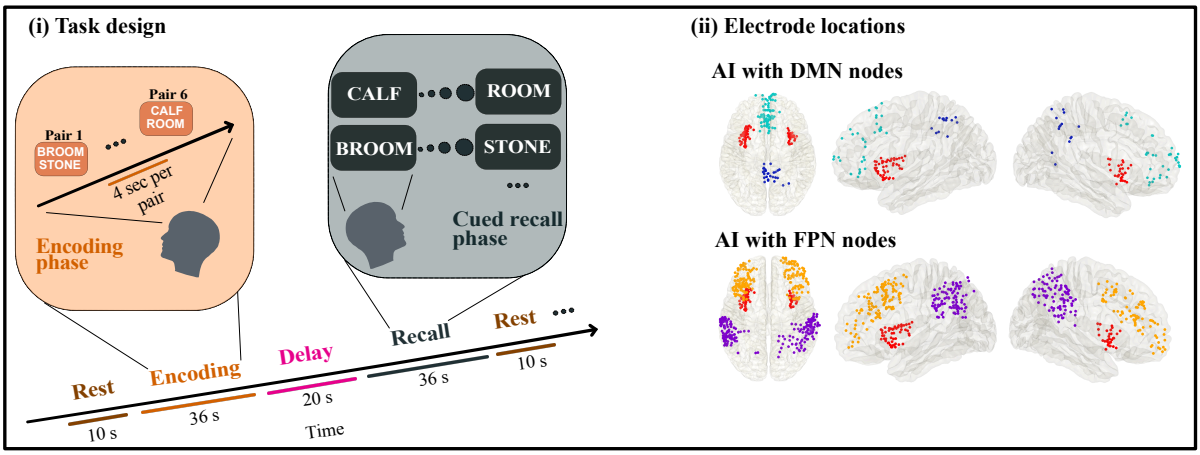

(d) Experiment 4 — WMSM

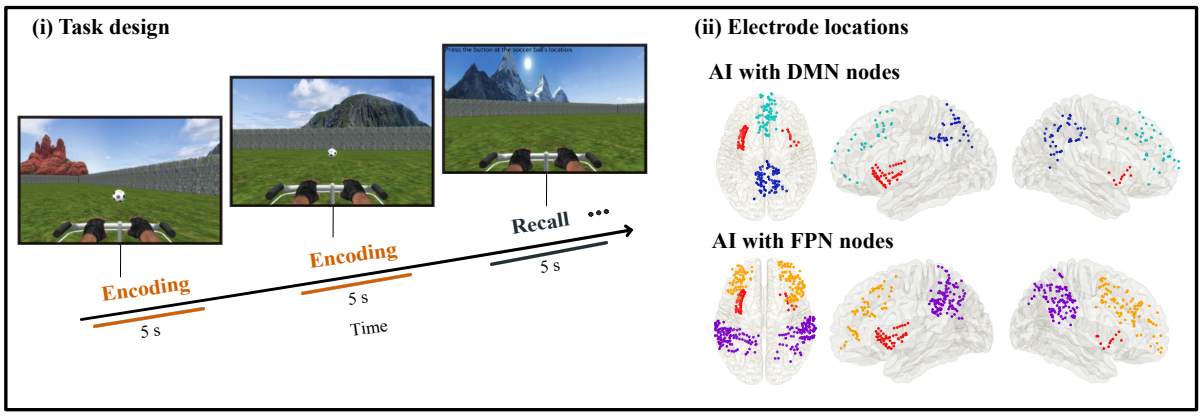

Figure 2.

(a) Experiment 1 — VFR

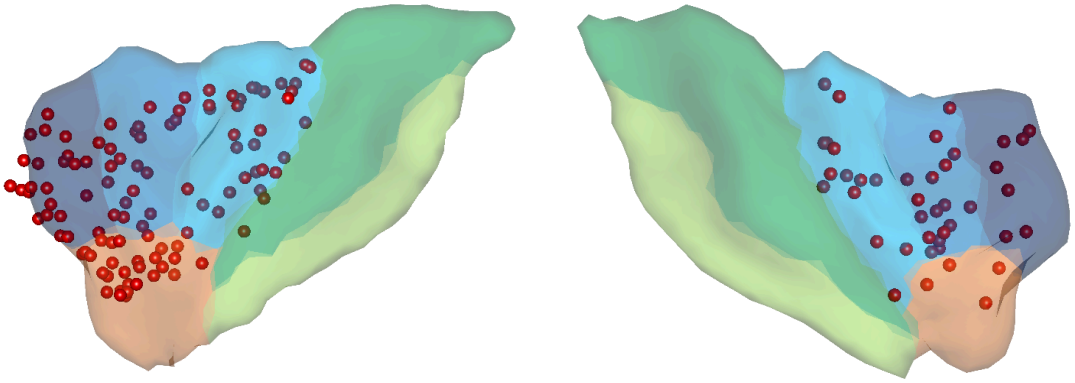

(b) Experiment 2 — CATVFR

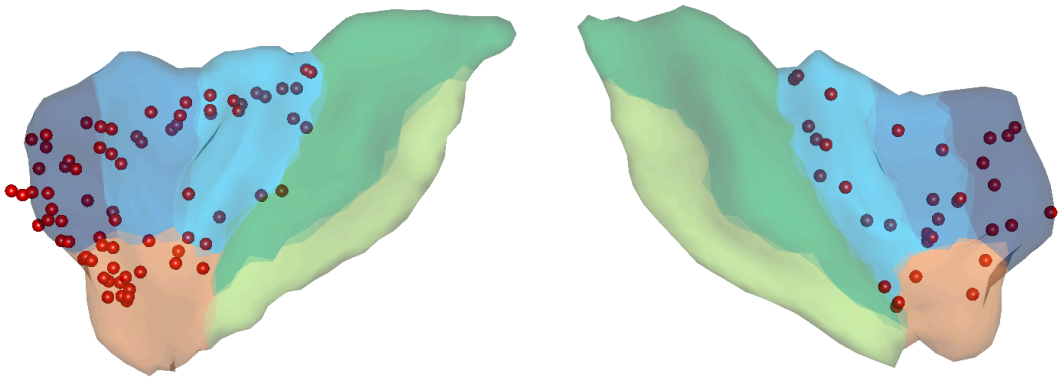

(c) Experiment 3 — PALVCR

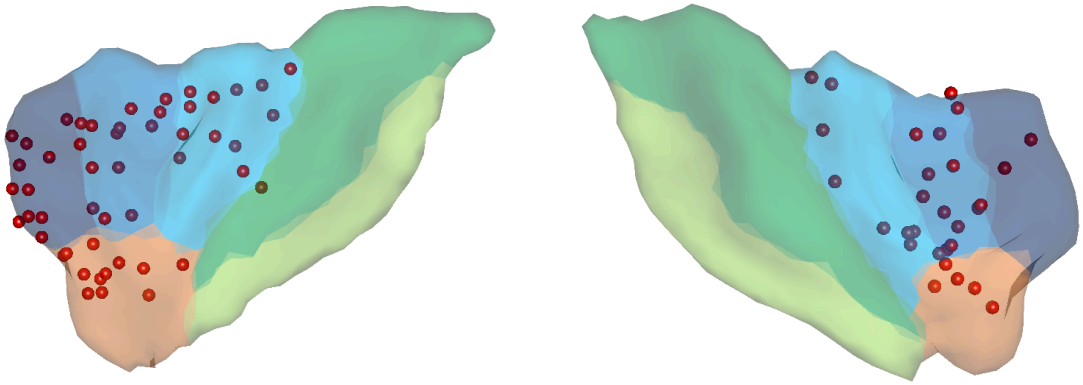

(d) Experiment 4 — WMSM

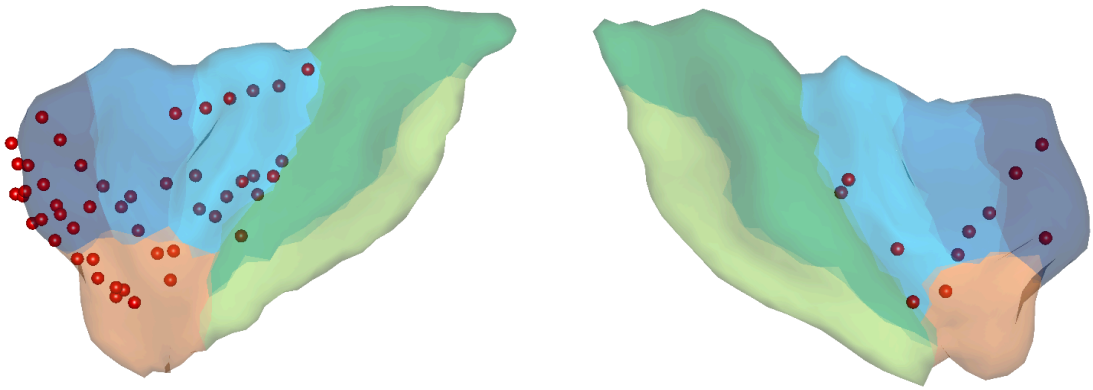

Figure 3.

(a) Experiment 1 — VFR

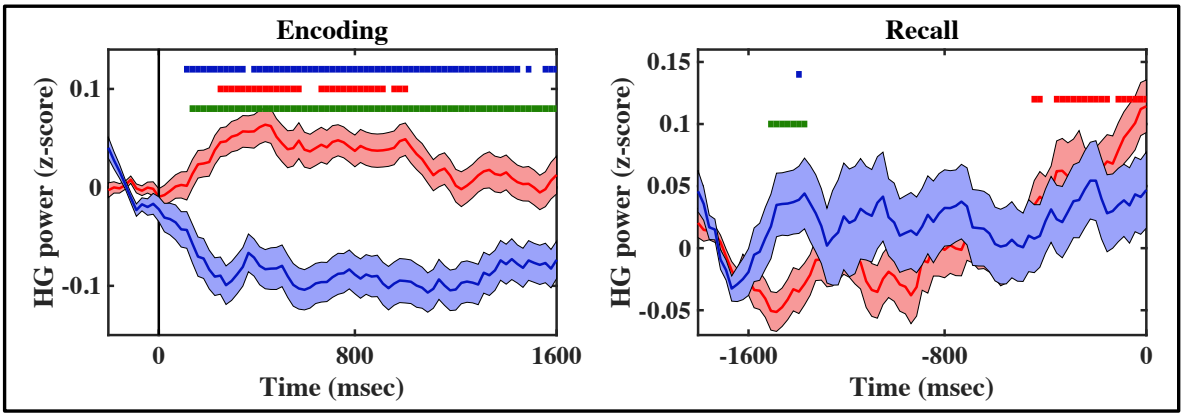

(b) Experiment 2 — CATVFR

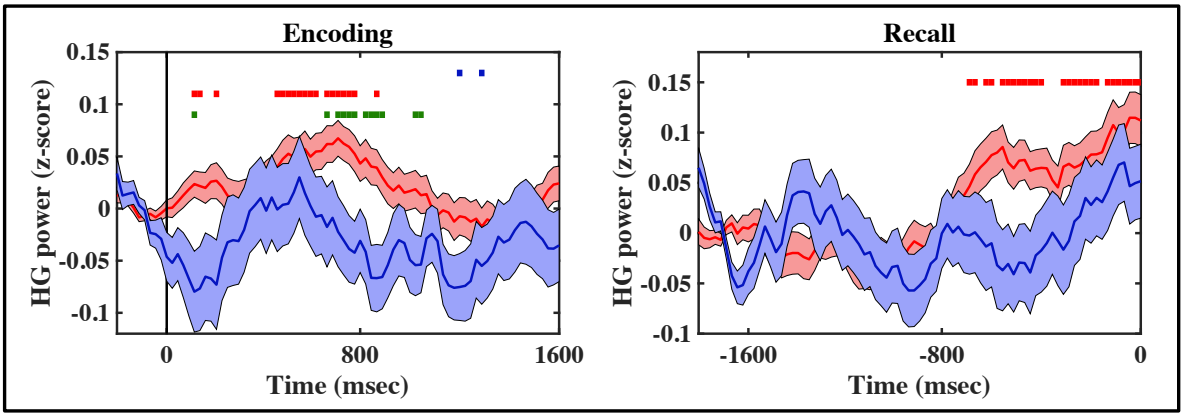

(c) Experiment 3 — PALVCR

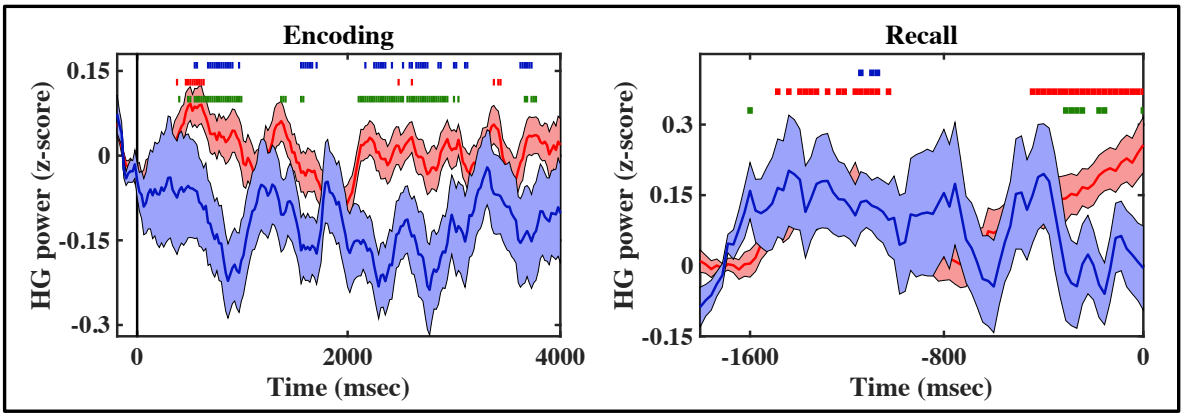

(d) Experiment 4 — WMSM

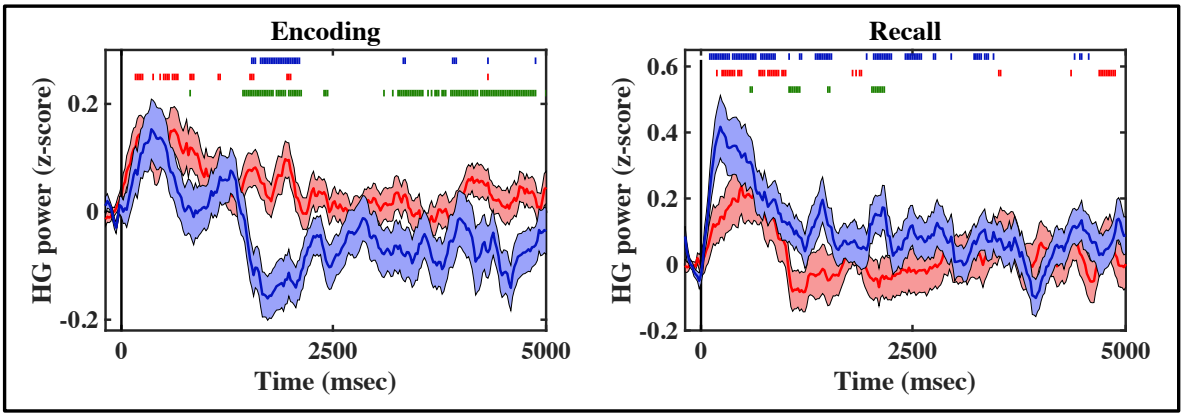

Figure 4.

(a) Experiment 1 — VFR

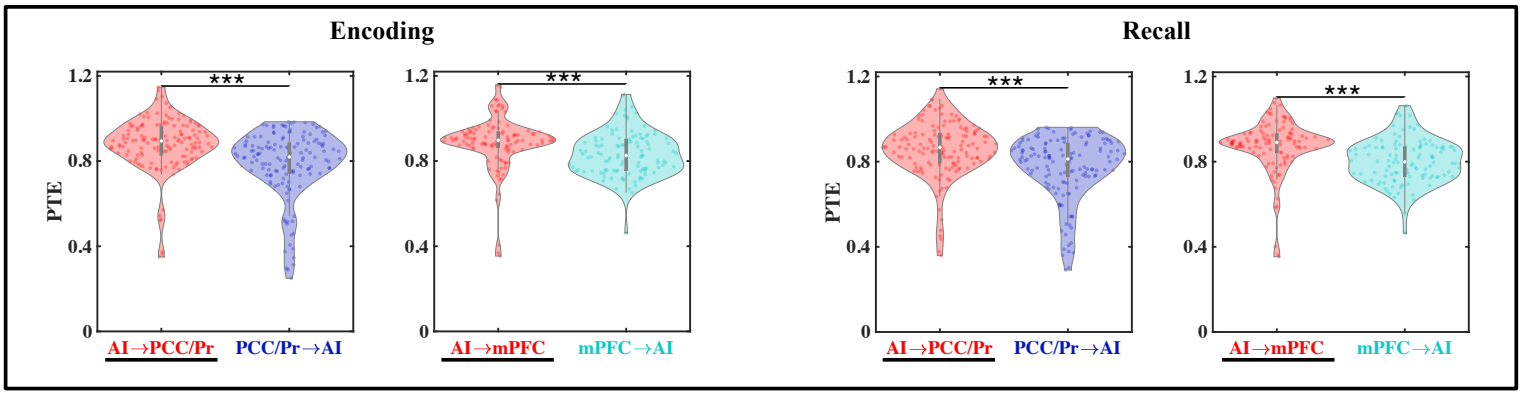

(b) Experiment 2 — CATVFR

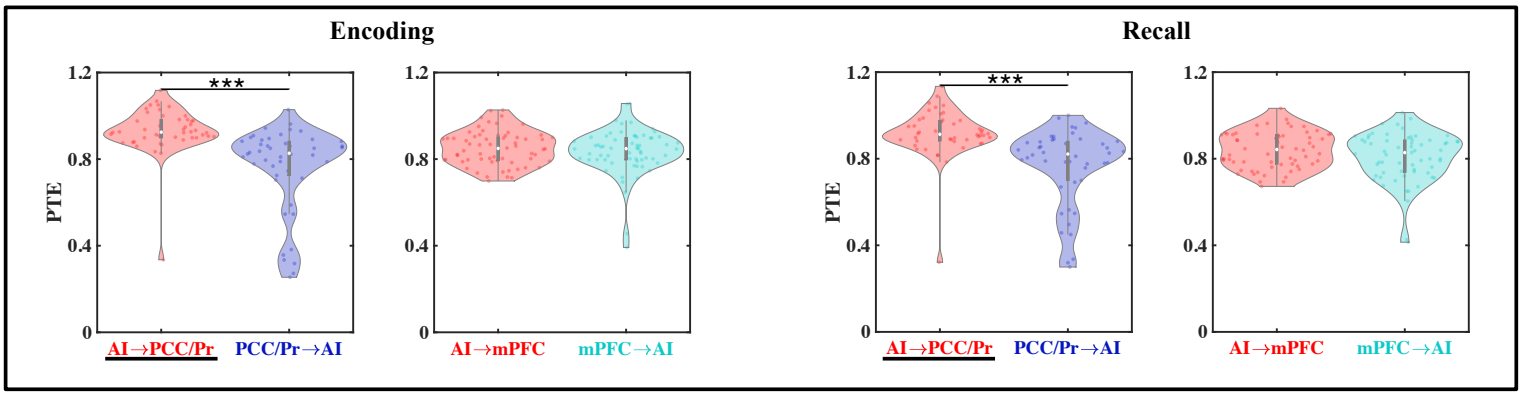

(c) Experiment 3 — PALVCR

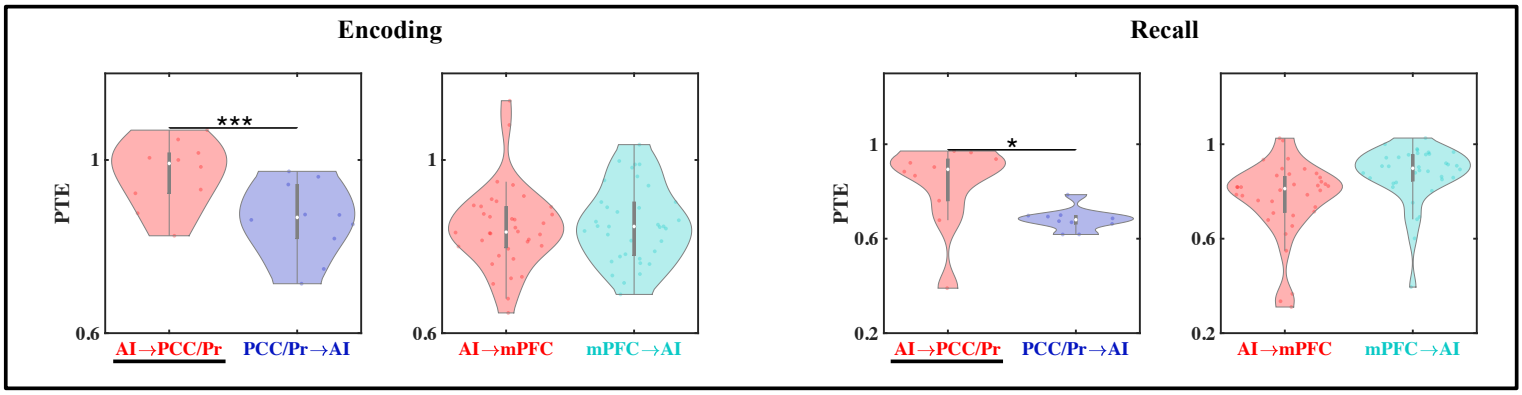

(d) Experiment 4 — WMSM

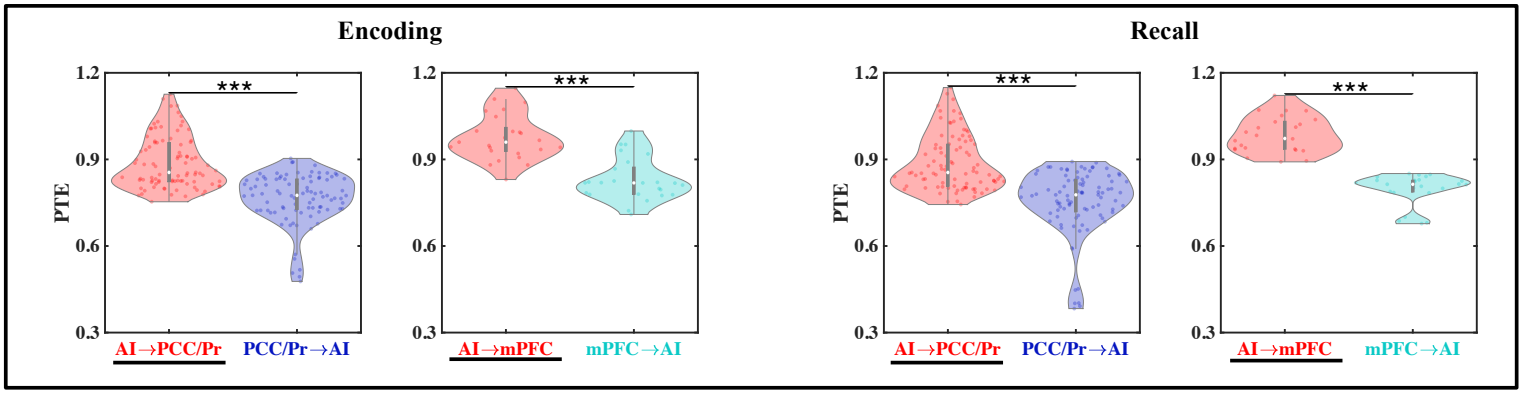

Figure 5.

(a) Experiment 1 — VFR

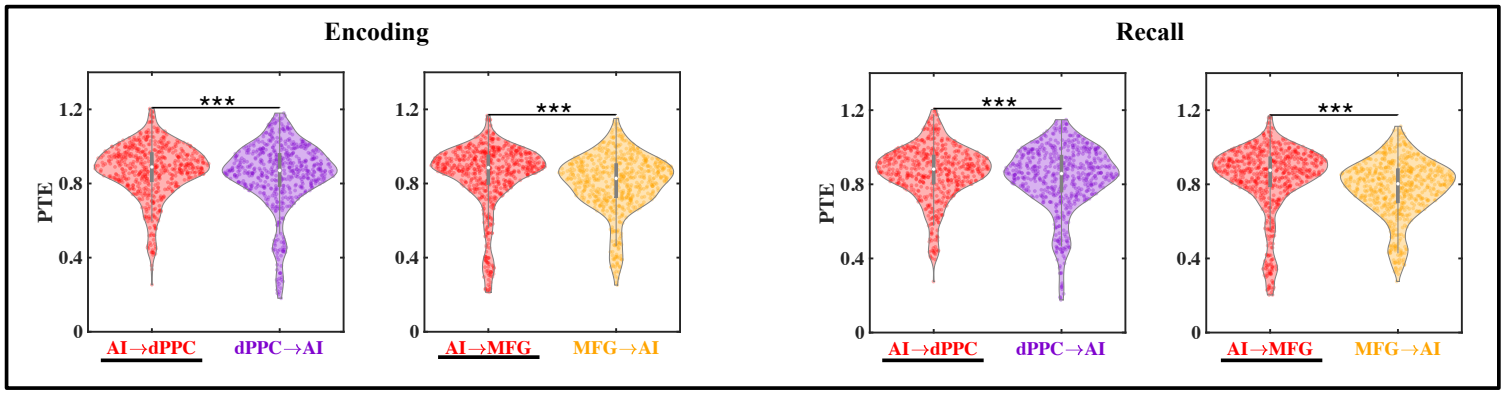

(b) Experiment 2 — CATVFR

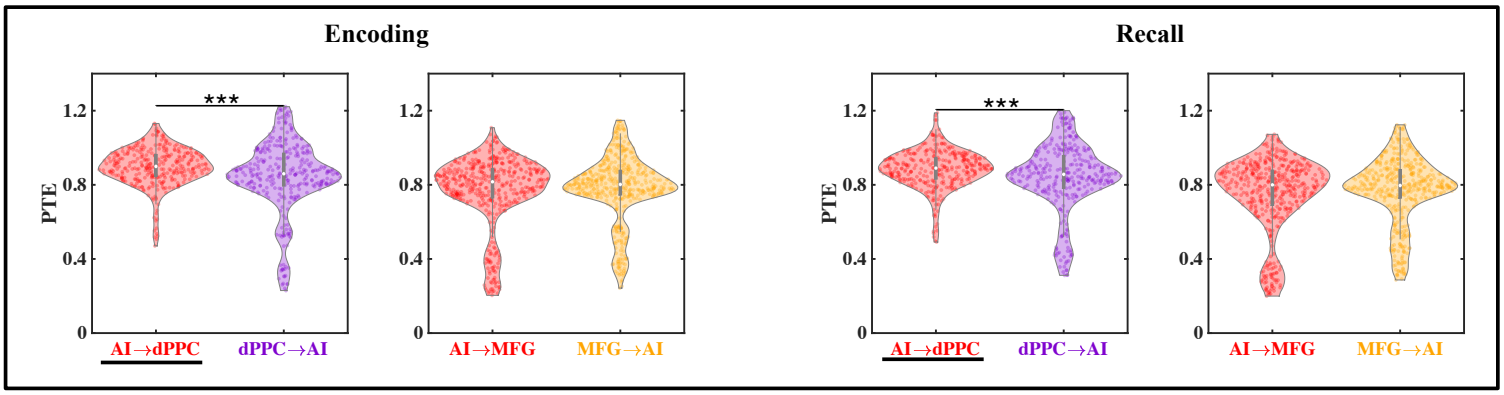

(c) Experiment 3 — PALVCR

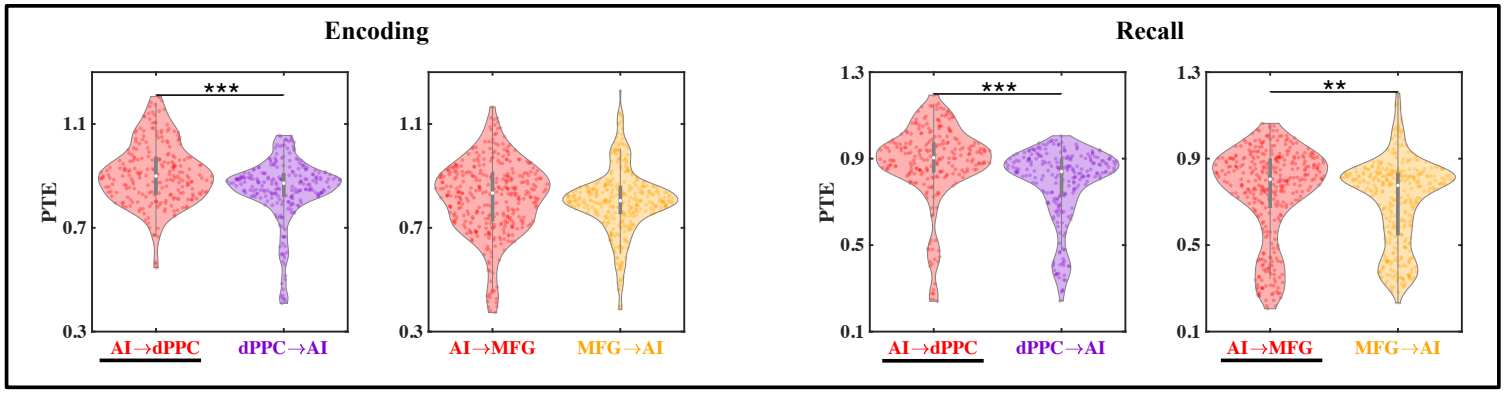

(d) Experiment 4 — WMSM

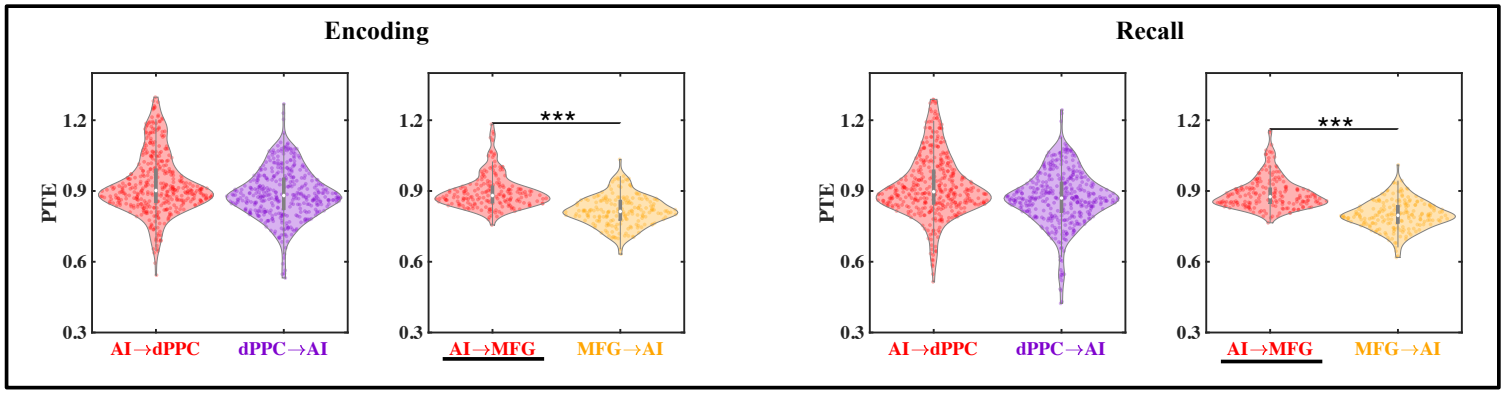

Figure 6.

(a) Experiment 1 — VFR

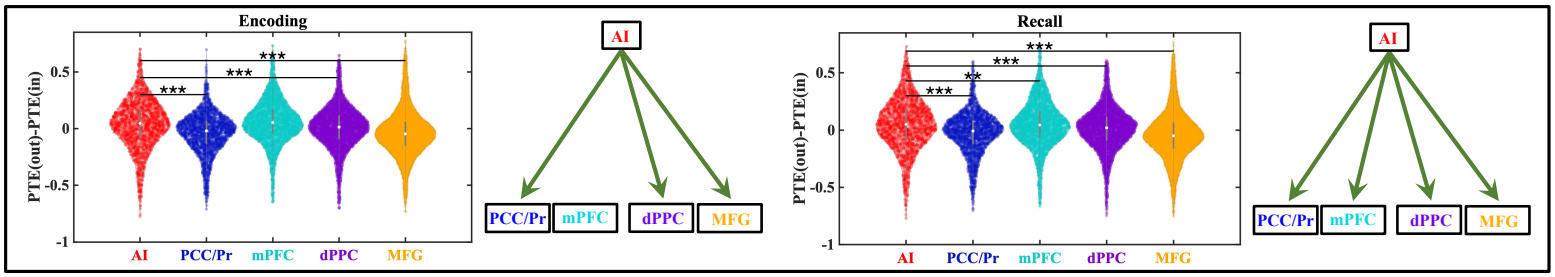

(b) Experiment 2 — CATVFR

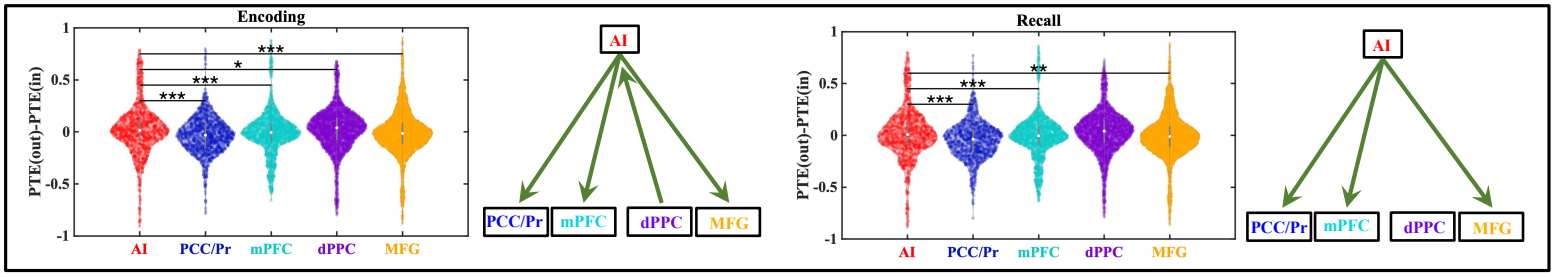

(c) Experiment 3 — PALVCR

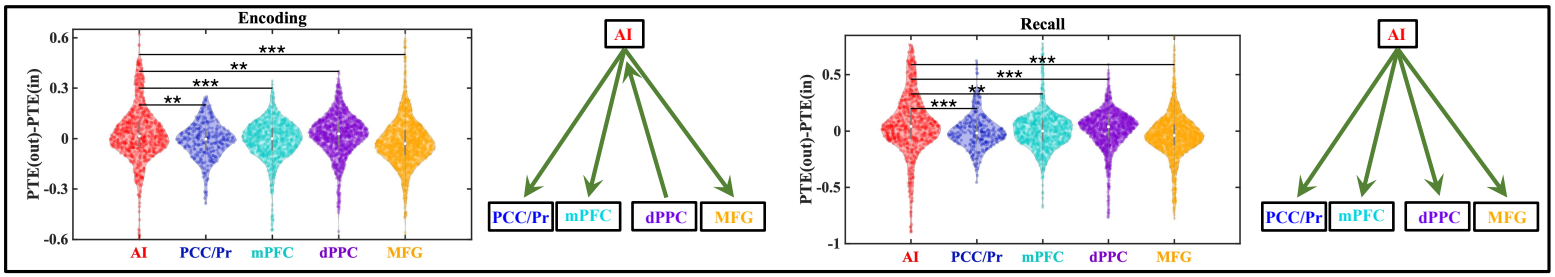

(d) Experiment 4 — WMSM

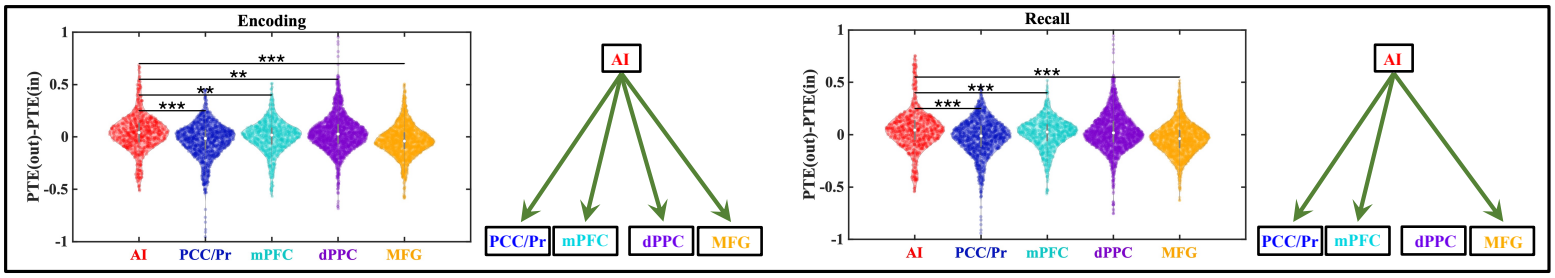

Figure 7.

(a) High-gamma response

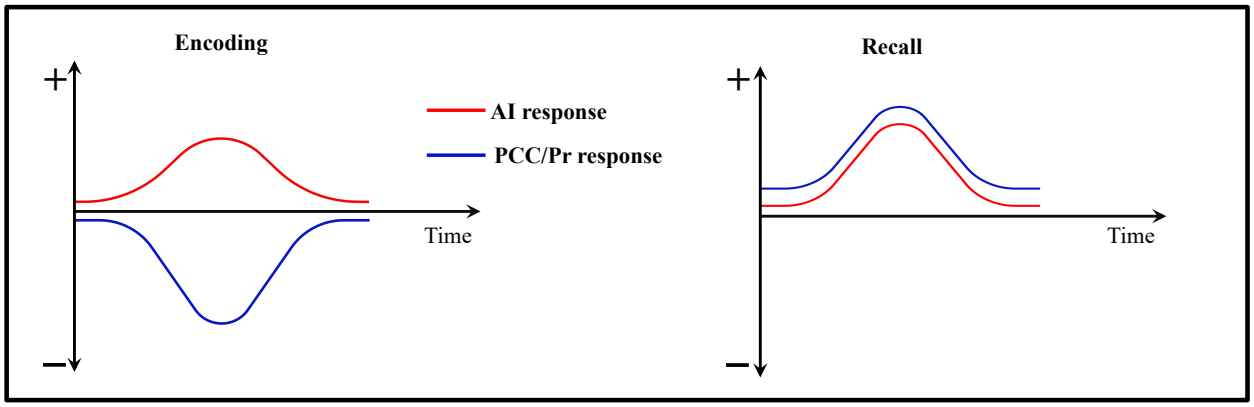

(b) Directed information flow

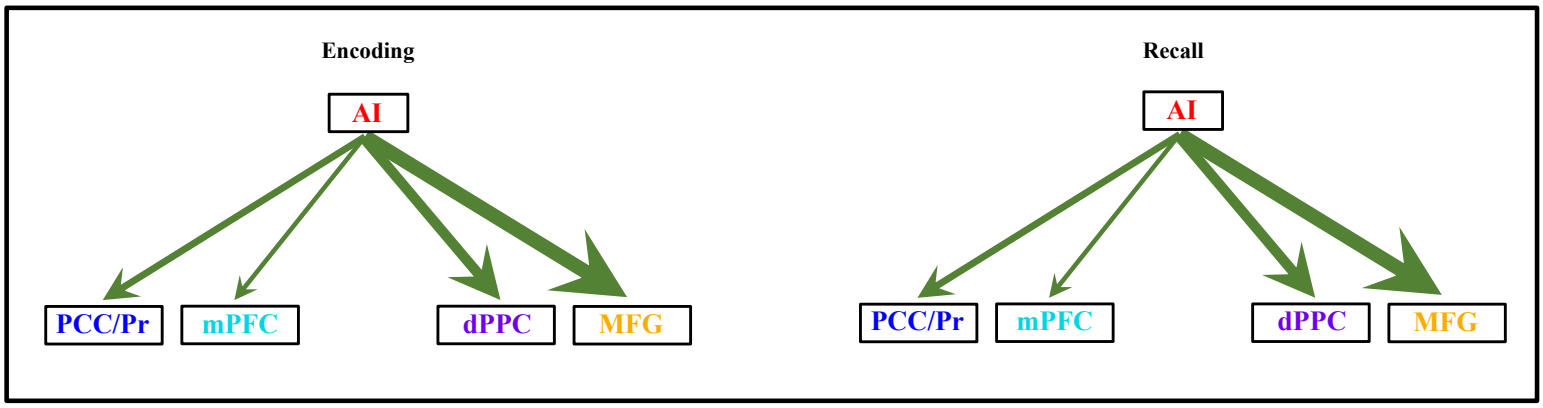

Supplementary Materials

I. Supplementary Figures (pages 2-6)

II. Supplementary Results (pages 7-10)

III. Supplementary Tables (pages 11-25)

Figure S1. iEEG evoked response for AI (red) and mPFC (cyan) in the four experiments. Green horizontal lines denote time periods where high-gamma power between the AI and mPFC were significantly different from each other. Red and cyan horizontal lines denote increase of high-gamma power compared to the resting baseline in the AI and mPFC respectively.

(a) Experiment 1 — VFR

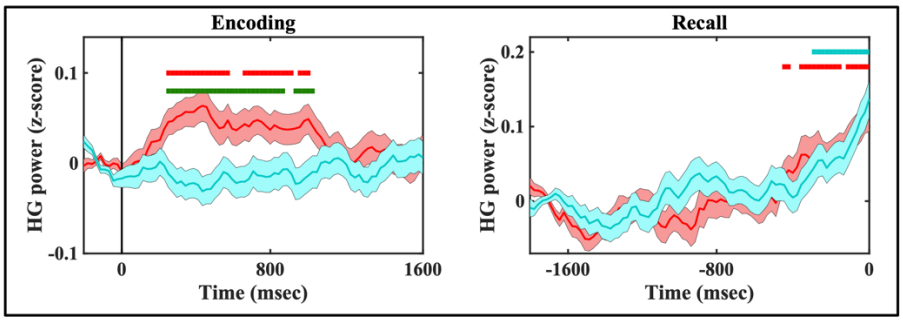

(b) Experiment 2 — CATVFR

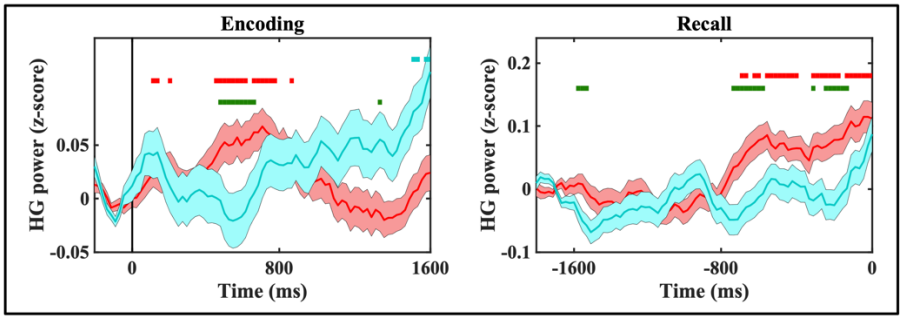

(c) Experiment 3 — PALVCR

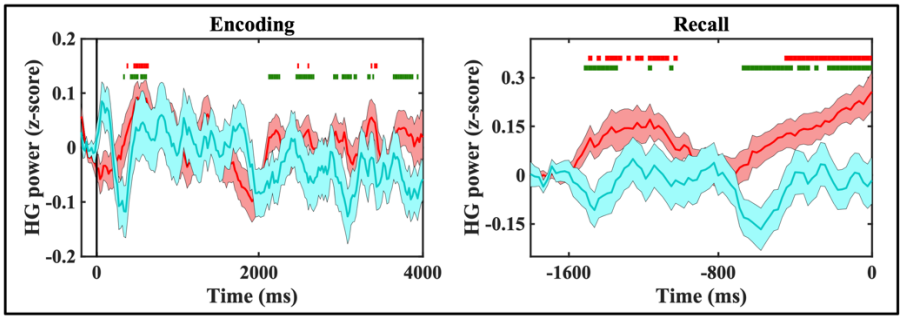

(d) Experiment 4 — WMSM

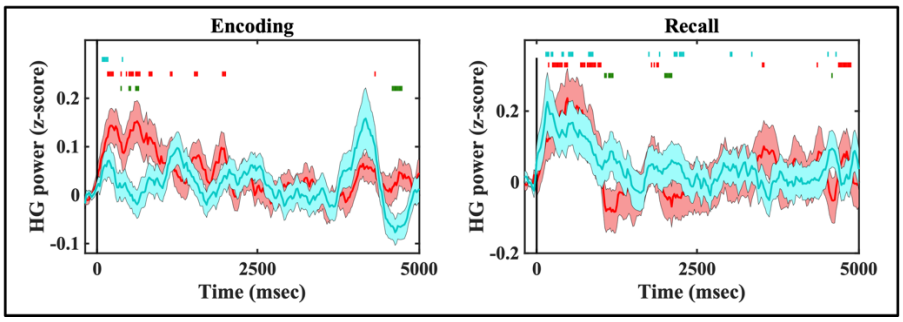

Figure S2. iEEG evoked response for AI (red) and dPPC (purple) in the four experiments. Green horizontal lines denote time periods where high-gamma power between the AI and dPPC were significantly different from each other. Red and purple horizontal lines denote increase of high-gamma power compared to the resting baseline in the AI and dPPC respectively.

(a) Experiment 1 — VFR

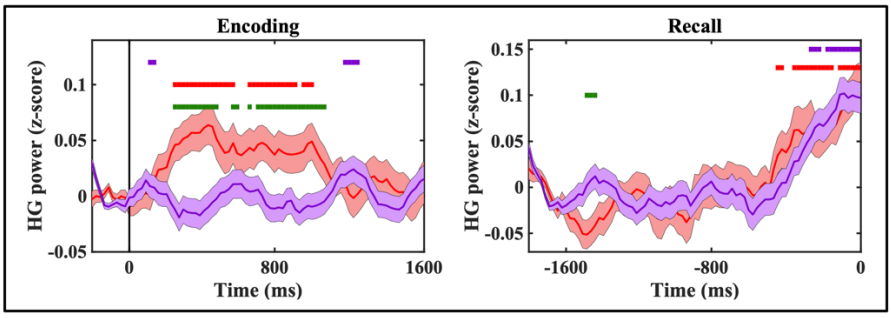

(b) Experiment 2 — CATVFR

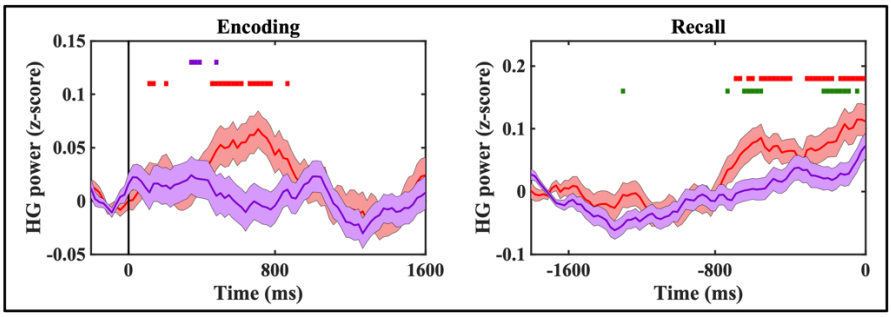

(c) Experiment 3 — PALVCR

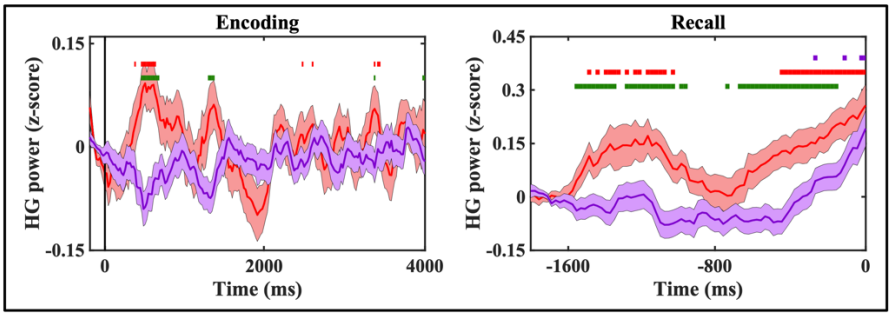

(d) Experiment 4 — WMSM

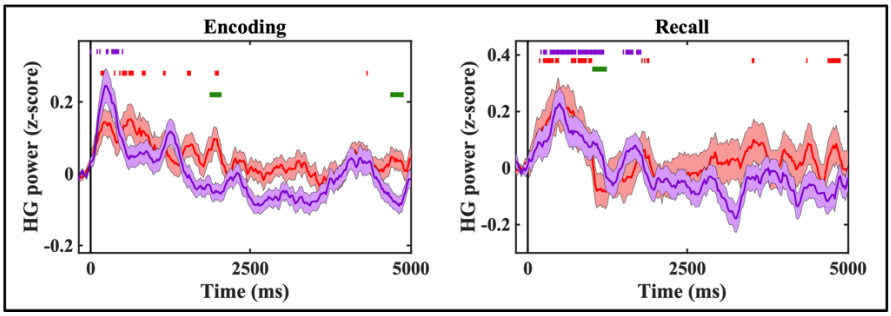

Figure S3. iEEG evoked response for AI (red) and MFG (orange) in the four experiments. Green horizontal lines denote time periods where high-gamma power between the AI and MFG were significantly different from each other. Red and orange horizontal lines denote increase of high-gamma power compared to the resting baseline in the AI and MFG respectively.

(a) Experiment 1 — VFR

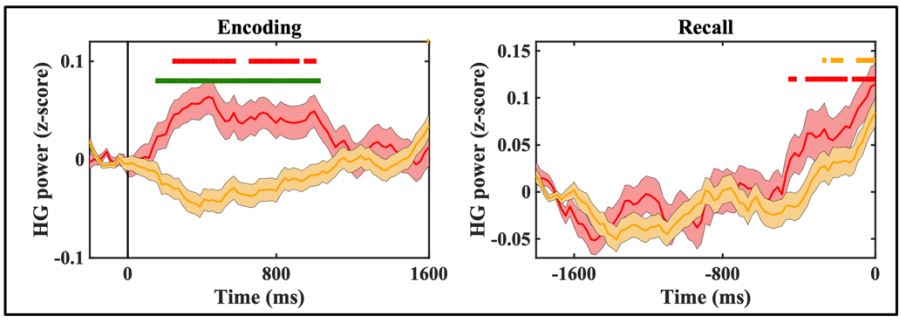

(b) Experiment 2 — CATVFR

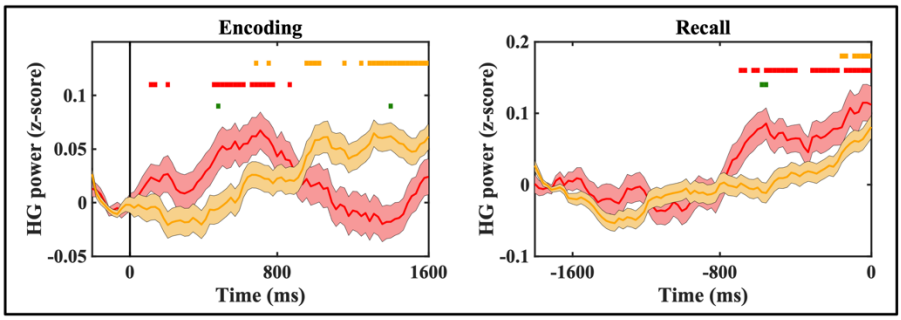

(c) Experiment 3 — PALVCR

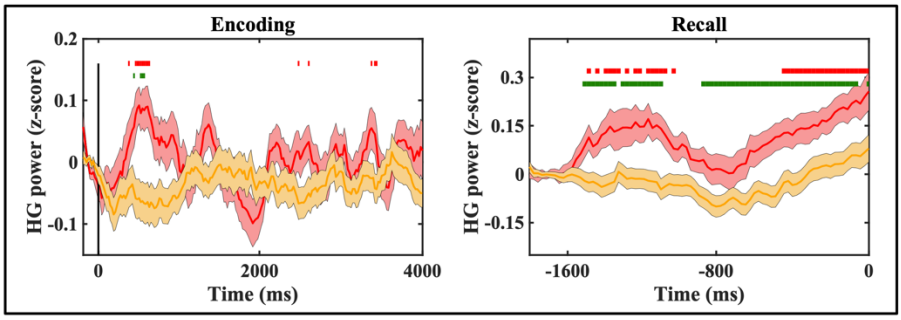

(d) Experiment 4 — WMSM

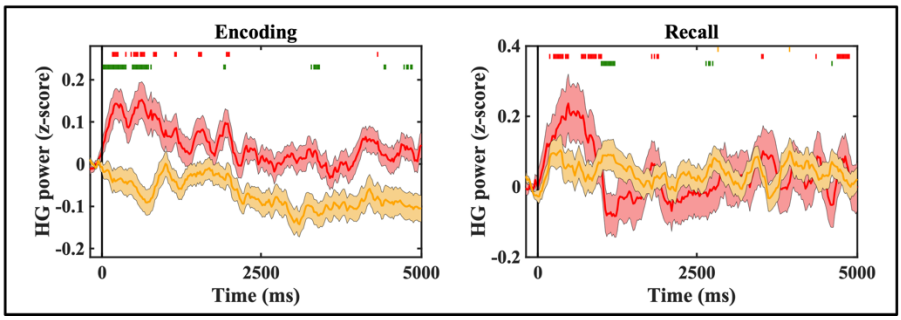

Figure S4. Differential directed information flow from the anterior insula to the DMN nodes during task versus resting-state, in broadband. *** $p < 0.001$, ** $p < 0.01$, * $p < 0.05$.

(a) Experiment 1 — VFR

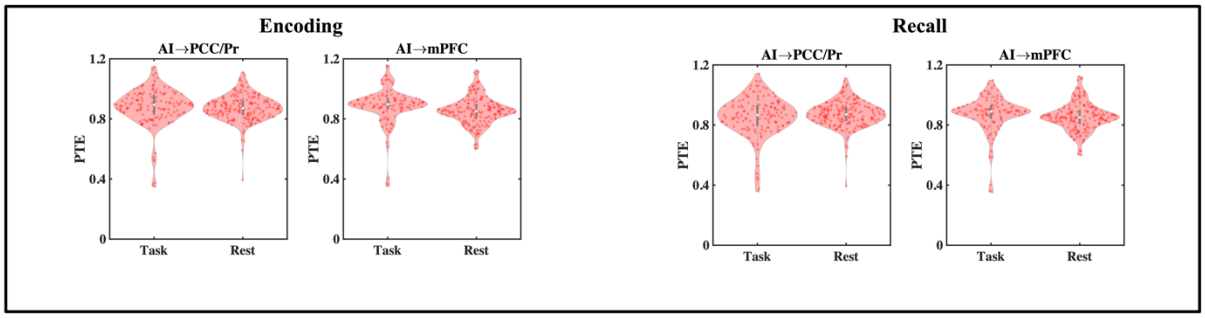

(b) Experiment 2 — CATVFR

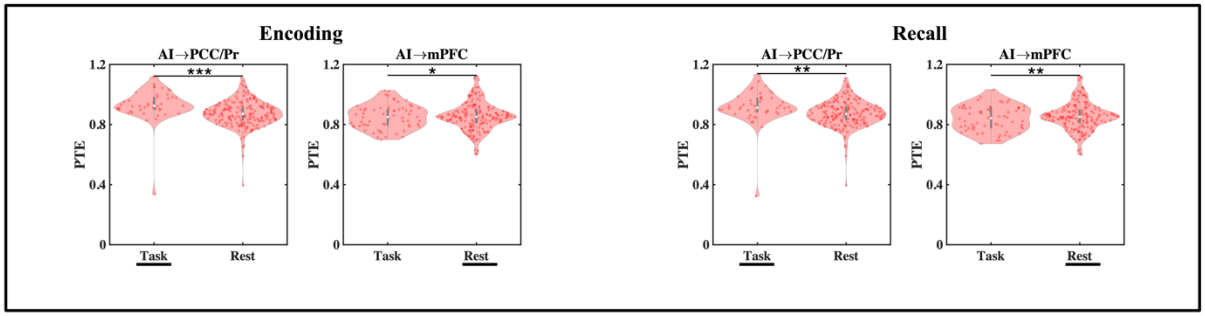

(c) Experiment 3 — PALVCR

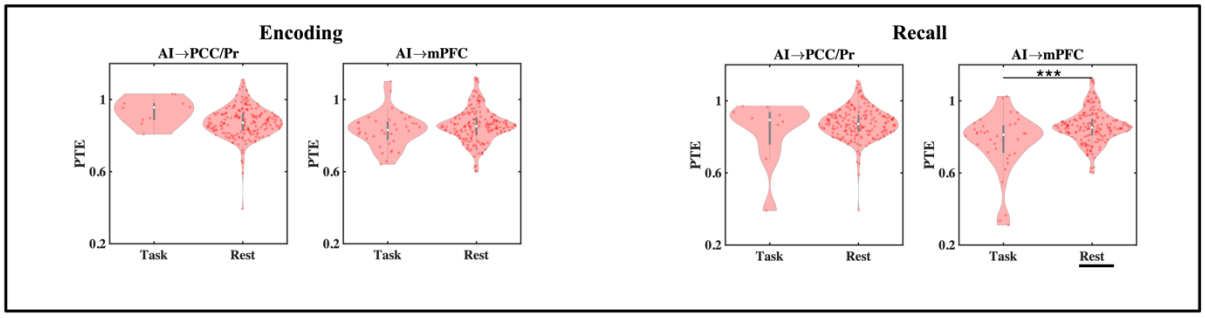

(d) Experiment 4 — WMSM

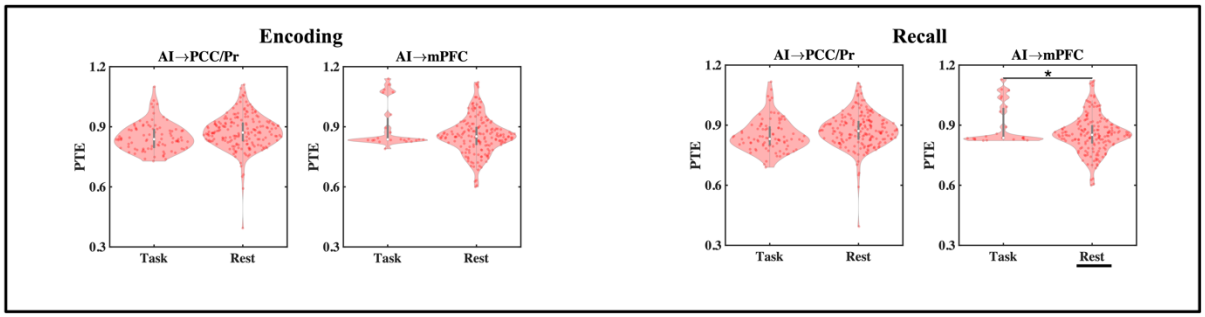

Figure S5. Differential directed information flow from the anterior insula to the FPN nodes during task versus resting-state, in broadband. *** $p < 0.001$, ** $p < 0.01$, * $p < 0.05$.

(a) Experiment 1 — VFR

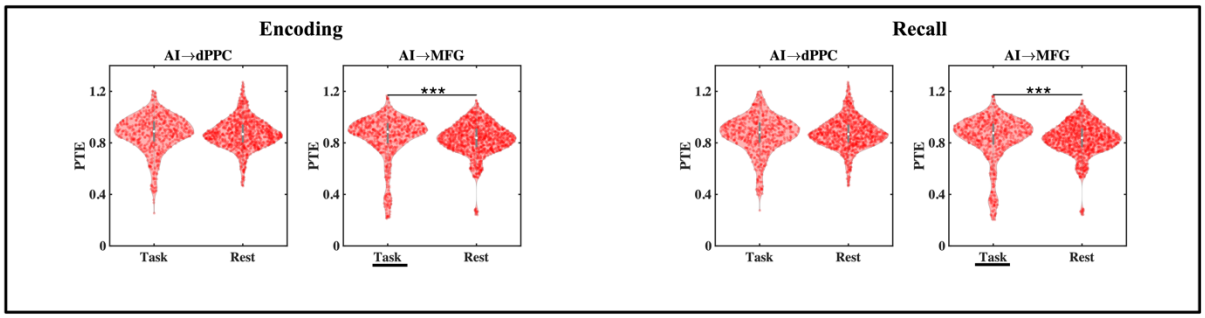

(b) Experiment 2 — CATVFR

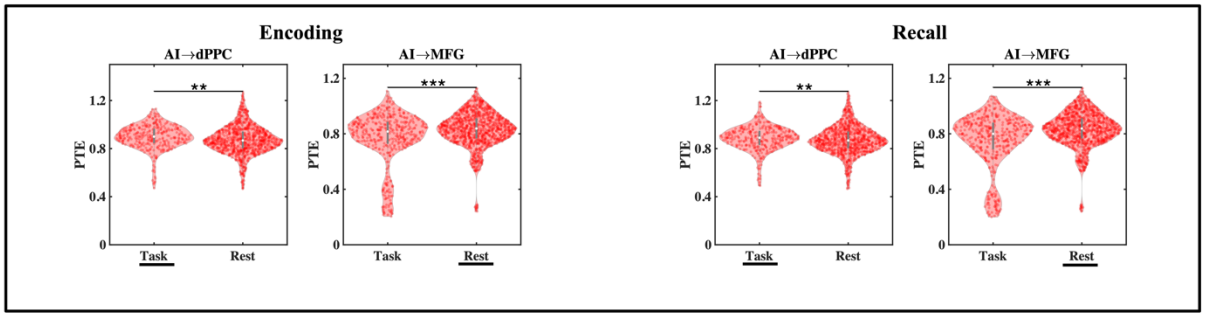

(c) Experiment 3 — PALVCR

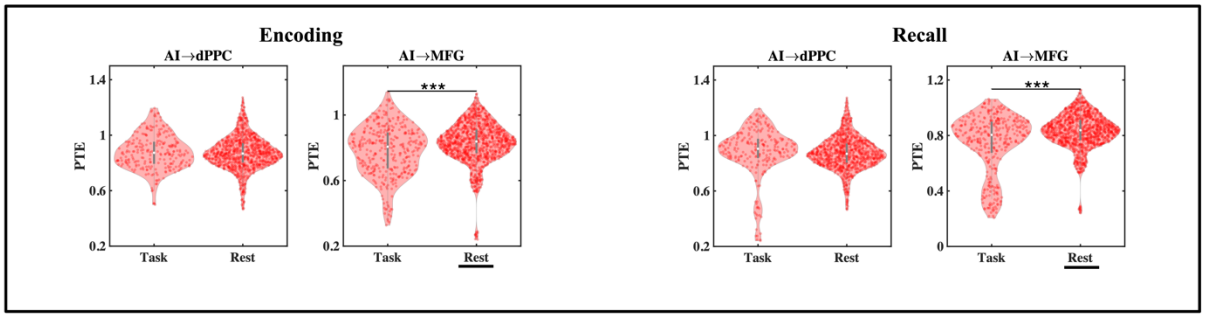

(d) Experiment 4 — WMSM

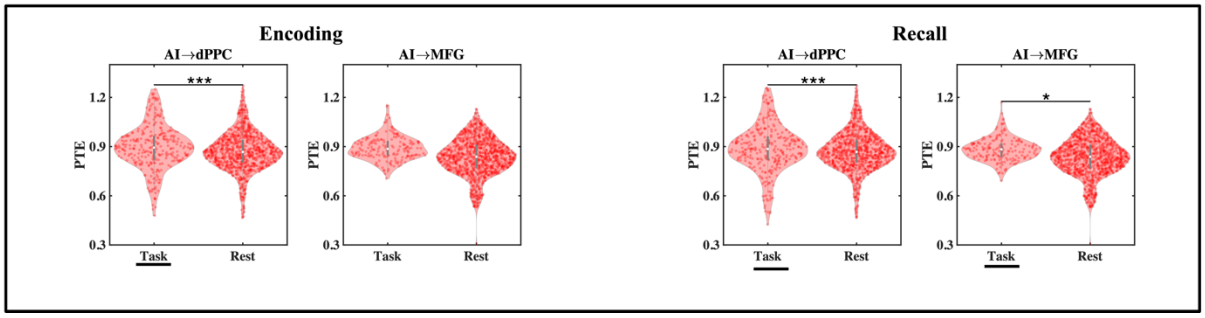

Supplementary Results

Causal information flow from the AI to the DMN during encoding and recall in the CATVFR task

Encoding Directed information flow from the AI to the PCC/precuneus was higher than the reverse, during memory encoding ($F(1, 84) = 36.18$, $p<0.001$, Cohen's $d = 1.32$) (**Figure 4b**).

Recall Directed information flow from the AI to the PCC/precuneus ($F(1, 83) = 29.54$, $p<0.001$, Cohen's $d = 1.19$) was higher, than the reverse, during memory recall (**Figure 4b**).

These results demonstrate that the AI has strong causal information flow to the PCC/precuneus node of the DMN during both the encoding and recall phases of the CATVFR episodic memory task.

Causal information flow from the AI to the DMN during encoding and recall in the PALVCR task

Encoding Directed information flow from the AI to the PCC/precuneus ($F(1, 17) = 22.19$, $p<0.001$, Cohen's $d = 2.28$) was higher, than the reverse (**Figure 4c**).

Recall Directed information flow from the AI to the PCC/precuneus was higher, than the reverse ($F(1, 17) = 6.45$, $p<0.05$, Cohen's $d = 1.23$) (**Figure 4c**).

These results demonstrate that the AI has stronger causal information flow to the PCC/precuneus node of the DMN during both the encoding and recall phases of the PALVCR episodic memory task.

Causal information flow from the AI to the DMN during encoding and recall in the WMSM task

Encoding Directed information flow from the AI to the PCC/precuneus ($F(1, 176) = 51.14$, $p<0.001$, Cohen's $d = 1.08$) and mPFC ($F(1, 41) = 44.53$, $p<0.001$, Cohen's $d = 2.08$) were higher, than the reverse (**Figure 4d**).

Recall Directed information flow from the AI to the PCC/precuneus ($F(1, 177) = 36.86$, $p<0.001$, Cohen's $d = 0.91$) and the mPFC ($F(1, 41) = 39.62$, $p<0.001$, Cohen's $d = 1.96$) were also higher, than the reverse (**Figure 4d**).

These results demonstrate that the AI has stronger causal information flow to the PCC/precuneus and mPFC nodes of the DMN during both the encoding and recall phases of the WMSM task.

Causal information flow from AI to FPN nodes in the CATVFR task

We next examined directed information flow between the AI and FPN nodes during the categorized verbal free recall task.

Encoding Directed information flow from the AI to the dPPC was higher, than the reverse ($F(1, 639) = 27.16$, $p<0.001$, Cohen's $d = 0.41$) (**Figure 5b**).

Recall Directed information flow from the AI to the dPPC was higher, than the reverse ($F(1, 639) = 20.48$, $p<0.001$, Cohen's $d = 0.36$) (**Figure 5b**).

These results demonstrate that the AI has stronger causal information flow to the dPPC node of the FPN during both the encoding and recall phases of the CATVFR episodic memory task.

Causal information flow from AI to FPN nodes in the PALVCR task

We next examined directed information flow between the AI and FPN nodes during the paired associates learning verbal cued recall task.

Encoding Directed information flow from the AI to the dPPC ($F(1, 476) = 38.25$, $p<0.001$, Cohen's $d = 0.57$) was higher, than the reverse (**Figure 5c**).

Recall Directed information flow from the AI to the dPPC ($F(1, 475) = 60.09$, $p<0.001$, Cohen's $d = 0.71$) and MFG ($F(1, 709) = 9.90$, $p<0.01$, Cohen's $d = 0.24$) were higher, than the reverse (**Figure 5c**).

These results demonstrate that the AI has stronger causal information flow to the dPPC node of the FPN during encoding and both dPPC and MFG nodes of the FPN during the recall phase of the PALVCR episodic memory task.

Causal information flow from the AI to FPN nodes in the WMSM task

Encoding Directed information flow from the AI to the MFG ($F(1, 343) = 74.38$, $p<0.001$, Cohen's $d = 0.93$) was higher, than the reverse (**Figure 5d**).

Recall Directed information flow from the AI to the MFG ($F(1, 344) = 102.18$, $p<0.001$, Cohen's $d = 1.09$) was higher, than the reverse (**Figure 5d**).

These results demonstrate that the AI has stronger causal information flow to the MFG node of the FPN during both the encoding and recall phases of the WMSM task.

Causal outflow hub during encoding and recall in the CATVFR task

Encoding Net causal outflow from the AI is positive and higher than both PCC/precuneus ($F(1, 2023) = 59.97$, $p<0.001$, Cohen's $d = 0.34$) and mPFC ($F(1, 2676) = 23.16$, $p<0.001$, Cohen's $d = 0.19$) during encoding (**Figure 6b**).

We also found that the net causal outflow from the AI is higher than the MFG during encoding ($F(1, 3974) = 11.61$, $p<0.001$, Cohen's $d = 0.11$) (**Figure 6b**). However, the net causal outflow

from the AI was lower than the dPPC during encoding ($F(1, 3535) = 6.04$, $p<0.05$, Cohen's $d = 0.08$) (**Figure 6b**).

Recall Net causal outflow from the AI is positive and higher than both PCC/precuneus ($F(1, 1827) = 33.55$, $p<0.001$, Cohen's $d = 0.27$) and mPFC ($F(1, 2656) = 29.81$, $p<0.001$, Cohen's $d = 0.21$) during the recall phase of the categorized verbal free recall task (**Figure 6b**).

We also found that the net causal outflow from the AI is higher than the MFG during recall ($F(1, 3827) = 6.87$, $p<0.01$, Cohen's $d = 0.08$) (**Figure 6b**).

Causal outflow hub during encoding and recall in the PALVCR task

Encoding We found similar results for the paired associates learning verbal cued recall task where, net causal outflow from the AI is positive and higher than both PCC/precuneus ($F(1, 736) = 9.84$, $p<0.01$, Cohen's $d = 0.23$) and mPFC ($F(1, 1079) = 21.93$, $p<0.001$, Cohen's $d = 0.29$) during memory encoding (**Figure 6c**).

We also found that the net causal outflow from the AI is higher than the MFG during encoding ($F(1, 1779) = 14.45$, $p<0.001$, Cohen's $d = 0.18$) (**Figure 6c**). However, the net causal outflow from the AI is lower than the dPPC during encoding ($F(1, 1261) = 8.72$, $p<0.01$, Cohen's $d = 0.17$) (**Figure 6c**).

Recall Net causal outflow from the AI is positive and higher than both PCC/precuneus ($F(1, 530) = 10.96$, $p<0.001$, Cohen's $d = 0.29$) and mPFC ($F(1, 909) = 8.42$, $p<0.01$, Cohen's $d = 0.19$) during memory recall (**Figure 6c**).

Net causal outflow from the AI is higher than both the dPPC ($F(1, 1041) = 31.15$, $p<0.001$, Cohen's $d = 0.35$) and MFG ($F(1, 736) = 70.08$, $p<0.001$, Cohen's $d = 0.62$) nodes of the FPN during the recall phase of the paired associates learning verbal cued recall task (**Figure 6c**).

Together, these results demonstrate that the AI is a causal outflow hub in its interactions with the PCC/precuneus and mPFC nodes of the DMN and the MFG node of the FPN, during both verbal memory encoding and recall.

Causal outflow hub during encoding and recall in the WMSM task

We next repeated our causal hub analysis during the encoding and recall phases of the water maze spatial memory task.

Encoding We found that net causal outflow from the AI is positive and higher than both the PCC/precuneus ($F(1, 1669) = 168.5$, $p<0.001$, Cohen's $d = 0.64$) and mPFC ($F(1, 1278) = 9.91$, $p<0.01$, Cohen's $d = 0.18$) nodes of the DMN during encoding (**Figure 6d**).

We also found that net causal outflow from the AI is higher than both the dPPC ($F(1, 2501) = 7.10$, $p<0.01$, Cohen's $d = 0.11$) and MFG ($F(1, 1977) = 73.49$, $p<0.001$, Cohen's $d = 0.39$) nodes of the FPN during encoding (**Figure 6d**).

Recall Net causal outflow from the AI is positive and higher than both the PCC/precuneus ($F(1, 1672) = 166.95$, $p<0.001$, Cohen's $d = 0.63$) and mPFC ($F(1, 1270) = 12.75$, $p<0.001$, Cohen's $d = 0.20$) nodes of the DMN during recall (**Figure 6d**).

Net causal outflow from the AI is also higher than the MFG ($F(1, 1985) = 90.81$, $p<0.001$, Cohen's $d = 0.43$) node of the FPN during recall (**Figure 6d**).

Together, these results demonstrate that the AI is a causal outflow hub in its interactions with the PCC/precuneus and mPFC nodes of the DMN and also the dPPC and MFG nodes of the FPN, during both spatial memory encoding and recall.

Supplementary Tables

Table S1. Participant demographic information (total 177 participants).

Participant ID	Gender	Age
001	F	48
002	F	49
003	F	39
006	F	20
010	F	30
014	F	47
015	F	54
018	M	47
019	F	34
020	F	48
021	M	38
022	M	24
023	M	32
024	F	36
025	F	19
026	F	24
027	M	48
028	F	27
029	F	33
030	M	23
032	F	19
033	F	31
034	F	29
035	F	45
036	M	49
039	F	28
041	M	34
042	F	28
044	M	58
045	M	51
049	F	52
050	M	20
051	F	24
052	F	19
053	F	39
054	M	23
056	M	34
057	M	53

059	F	44
060	F	36
062	F	23
063	M	23
064	M	56
065	F	34
066	M	39
067	F	45
068	F	39
069	M	26
070	F	40
074	M	24
075	M	50
076	M	29
077	F	47
078	F	22
080	F	43
081	F	33
082	M	39
084	M	25
087	M	51
089	M	36
090	F	52
091	M	28
092	M	44
093	M	24
094	M	47
095	F	35
097	M	34
098	F	38
100	F	43
101	F	26
102	M	34
105	M	25
106	M	26
107	M	25
108	F	23
109	F	43
111	M	20
114	F	31
115	M	47
118	M	33
119	F	26

120	F	33
121	M	34
123	F	29
124	F	40
125	F	44
127	F	40
128	M	26
129	F	34
130	M	57
131	M	24
134	M	64
135	M	47
136	F	16
137	F	21
138	M	41
141	F	44
142	F	43
144	M	53
147	M	47
148	F	59
149	F	28
150	F	49
151	M	36
153	M	38
155	M	37
156	M	27
157	M	22
158	F	45
159	F	42
161	F	53
162	F	30
163	M	45
164	M	37
166	M	38
167	M	33
168	M	24
171	M	36
172	F	22
173	F	18
174	M	29
175	M	34
176	F	41
177	F	23

178	M	40
180	F	21
181	M	22
184	M	42
186	M	27
187	F	51
189	M	22
190	F	57
193	M	37
195	M	44
196	M	18
200	M	25
202	F	29
203	F	36
204	F	25
207	F	39
212	M	46
221	M	57
222	F	20
223	F	42
227	M	32
228	F	58
230	F	56
232	M	27
234	M	25
236	F	51
238	M	27
239	M	27
240	F	37
245	M	30
247	F	61
251	M	31
260	F	57
263	M	30
264	F	52
268	F	32
271	M	37
274	F	44
275	M	41
276	M	28
279	F	57
283	F	29
284	F	32

286	F	57
292	F	39
297	M	24
298	F	24
299	M	43
302	M	48
303	F	62
304	F	33
310	M	20
312	M	21

Table S2a. Number of electrode pairs used in phase transfer entropy (PTE) analysis in the verbal free recall task. AI: anterior insula, PCC: posterior cingulate cortex, Pr: precuneus, mPFC: medial prefrontal cortex, dPPC: dorsal posterior parietal cortex, MFG: middle frontal gyrus.

Network pair	Number of electrode pairs (n)	Number of participants	Participant IDs (Gender/Age)
AI-PCC/Pr	142	18	030 (M/23), 049 (F/52), 054 (M/23), 057 (M/53), 062 (F/23), 114 (F/31), 115 (M/47), 134 (M/64), 153 (M/38), 158 (F/45), 168 (M/24), 193 (M/37), 196 (M/18), 204 (F/25), 236 (F/51), 240 (F/37), 286 (F/57), 299 (M/43)
AI-mPFC	112	20	026 (F/24), 027 (M/48), 049 (F/52), 057 (M/53), 062 (F/23), 114 (F/31), 115 (M/47), 123 (F/29), 153 (M/38), 163 (M/45), 168 (M/24), 189 (M/22), 193 (M/37), 196 (M/18), 204 (F/25), 223 (F/42), 228 (F/58), 247 (F/61), 274 (F/44), 299 (M/43)
AI-dPPC	586	28	030 (M/23), 032 (F/19), 033 (F/31), 049 (F/52), 054 (M/23), 057 (M/53), 062 (F/23), 065 (F/34), 080 (F/43), 114 (F/31), 115 (M/47), 128 (M/26), 134 (M/64), 153 (M/38), 158 (F/45), 163 (M/45), 168 (M/24), 173 (F/18), 189 (M/22), 193 (M/37), 196 (M/18), 204 (F/25), 232 (M/27), 236 (F/51), 240 (F/37), 247 (F/61), 286 (F/57), 299 (M/43)
AI-MFG	642	36	026 (F/24), 030 (M/23), 032 (F/19), 033 (F/31), 049 (F/52), 054 (M/23), 057 (M/53), 062 (F/23), 063 (M/23), 065 (F/34), 114 (F/31), 115 (M/47), 153 (M/38), 158 (F/45), 163 (M/45), 166 (M/38), 168 (M/24), 178 (M/40), 189 (M/22), 193 (M/37), 196 (M/18), 204 (F/25), 207 (F/39), 223 (F/42), 228 (F/58), 230 (F/56), 232 (M/27), 240 (F/37), 247 (F/61), 264 (F/52), 274 (F/44), 283 (F/29), 286 (F/57), 298 (F/24), 299 (M/43), 310 (M/20)

Table S2b. Number of electrode pairs used in phase transfer entropy (PTE) analysis in the categorized verbal free recall task. AI: anterior insula, PCC: posterior cingulate cortex, Pr: precuneus, mPFC: medial prefrontal cortex, dPPC: dorsal posterior parietal cortex, MFG: middle frontal gyrus.

Network pair	Number of electrode pairs (n)	Number of participants	Participant IDs (Gender/Age)
AI-PCC/Pr	46	7	114 (F/31), 141 (F/44), 158 (F/45), 204 (F/25), 240 (F/37), 245 (M/30), 286 (F/57)
AI-mPFC	64	12	026 (F/24), 114 (F/31), 141 (F/44), 163 (M/45), 189 (M/22), 204 (F/25), 228 (F/58), 245 (M/30), 247 (F/61), 271 (M/37), 274 (F/44), 303 (F/62)
AI-dPPC	327	14	028 (F/27), 032 (F/19), 065 (F/34), 114 (F/31), 141 (F/44), 158 (F/45), 163 (M/45), 189 (M/22), 204 (F/25), 240 (F/37), 245 (M/30), 247 (F/61), 271 (M/37), 286 (F/57)
AI-MFG	462	22	026 (F/24), 032 (F/19), 065 (F/34), 114 (F/31), 141 (F/44), 158 (F/45), 163 (M/45), 178 (M/40), 189 (M/22), 204 (F/25), 207 (F/39), 228 (F/58), 230 (F/56), 240 (F/37), 245 (M/30), 247 (F/61), 264 (F/52), 271 (M/37), 274 (F/44), 286 (F/57), 303 (F/62), 310 (M/20)

Table S2c. Number of electrode pairs used in phase transfer entropy (PTE) analysis in the paired associates learning verbal cued recall task. AI: anterior insula, PCC: posterior cingulate cortex, Pr: precuneus, mPFC: medial prefrontal cortex, dPPC: dorsal posterior parietal cortex, MFG: middle frontal gyrus.

Network pair	Number of electrode pairs (n)	Number of participants	Participant IDs (Gender/Age)
AI-PCC/Pr	10	2	141 (F/44), 196 (M/18)
AI-mPFC	36	5	141 (F/44), 196 (M/18), 223 (F/42), 228 (F/58), 303 (F/62)
AI-dPPC	242	9	028 (F/27), 065 (F/34), 090 (F/52), 091 (M/28), 141 (F/44), 196 (M/18), 232 (M/27), 238 (M/27), 312 (M/21)
AI-MFG	362	14	065 (F/34), 090 (F/52), 091 (M/28), 141 (F/44), 196 (M/18), 207 (F/39),

			223 (F/42), 228 (F/58), 230 (F/56), 232 (M/27), 238 (M/27), 283 (F/29), 303 (F/62), 312 (M/21)

Table S2d. Number of electrode pairs used in phase transfer entropy (PTE) analysis in the water maze spatial memory task. AI: anterior insula, PCC: posterior cingulate cortex, Pr: precuneus, mPFC: medial prefrontal cortex, dPPC: dorsal posterior parietal cortex, MFG: middle frontal gyrus.

Network pair	Number of electrode pairs (n)	Number of participants	Participant IDs (Gender/Age)
AI-PCC/Pr	91	6	030 (M/23), 049 (F/52), 054 (M/23), 062 (F/23), 114 (F/31), 124 (F/40)
AI-mPFC	23	5	026 (F/24), 049 (F/52), 052 (F/19), 062 (F/23), 114 (F/31)
AI-dPPC	302	10	030 (M/23), 032 (F/19), 033 (F/31), 049 (F/52), 052 (F/19), 054 (M/23), 062 (F/23), 065 (F/34), 114 (F/31), 124 (F/40)
AI-MFG	177	10	026 (F/24), 030 (M/23), 032 (F/19), 033 (F/31), 049 (F/52), 052 (F/19), 054 (M/23), 062 (F/23), 065 (F/34), 114 (F/31)

Table S3a. Number of electrodes in each node used in high-gamma power analysis in the verbal free recall task. AI: anterior insula, PCC: posterior cingulate cortex, Pr: precuneus, mPFC: medial prefrontal cortex, dPPC: dorsal posterior parietal cortex, MFG: middle frontal gyrus.

Brain regions	Number of electrodes (n)	Number of participants	Participant IDs (Gender/Age)
AI	148	44	026 (F/24), 027 (M/48), 030 (M/23), 032 (F/19), 033 (F/31), 049 (F/52), 054 (M/23), 057 (M/53), 062 (F/23), 063 (M/23), 065 (F/34), 080 (F/43), 114 (F/31), 115 (M/47), 123 (F/29), 128 (M/26), 134 (M/64), 150 (F/49), 153 (M/38), 158 (F/45), 163 (M/45), 166 (M/38), 168 (M/24), 173 (F/18), 178 (M/40), 189 (M/22), 193 (M/37), 196 (M/18), 204 (F/25), 207 (F/39), 223 (F/42), 228 (F/58), 230 (F/56), 232 (M/27), 236 (F/51), 240 (F/37),

			247 (F/61), 264 (F/52), 274 (F/44), 283 (F/29), 286 (F/57), 298 (F/24), 299 (M/43), 310 (M/20)
PCC/Pr	143	47	006 (F/20), 010 (F/30), 015 (F/54), 018 (M/47), 023 (M/32), 030 (M/23), 034 (F/29), 039 (F/28), 044 (M/58), 049 (F/52), 051 (F/24), 054 (M/23), 057 (M/53), 062 (F/23), 070 (F/40), 074 (M/24), 076 (M/29), 077 (F/47), 081 (F/33), 084 (M/25), 094 (M/47), 101 (F/26), 105 (M/25), 106 (M/26), 114 (F/31), 115 (M/47), 134 (M/64), 135 (M/47), 138 (M/41), 153 (M/38), 155 (M/37), 158 (F/45), 162 (F/30), 168 (M/24), 175 (M/34), 186 (M/27), 193 (M/37), 196 (M/18), 203 (F/36), 204 (F/25), 236 (F/51), 240 (F/37), 268 (F/32), 275 (M/41), 286 (F/57), 297 (M/24), 299 (M/43)
mPFC	312	55	018 (M/47), 022 (M/24), 026 (F/24), 027 (M/48), 034 (F/29), 036 (M/49), 039 (F/28), 049 (F/52), 051 (F/24), 053 (F/39), 056 (M/34), 057 (M/53), 059 (F/44), 060 (F/36), 062 (F/23), 070 (F/40), 074 (M/24), 075 (M/50), 077 (F/47), 081 (F/33), 084 (M/25), 098 (F/38), 106 (M/26), 114 (F/31), 115 (M/47), 121 (M/34), 123 (F/29), 129 (F/34), 130 (M/57), 131 (M/24), 142 (F/43), 151 (M/36), 153 (M/38), 155 (M/37), 156 (M/27), 163 (M/45), 167 (M/33), 168 (M/24), 175 (M/34), 187 (F/51), 189 (M/22), 193 (M/37), 196 (M/18), 200 (M/25), 202 (F/29), 203 (F/36), 204 (F/25), 222 (F/20), 223 (F/42), 228 (F/58), 247 (F/61), 274 (F/44), 275 (M/41), 299 (M/43), 304 (F/33)
dPPC	537	89	001 (F/48), 003 (F/39), 006 (F/20), 010 (F/30), 015 (F/54), 018 (M/47), 020 (F/48), 023 (M/32), 030 (M/23), 032 (F/19), 033 (F/31), 035 (F/45), 036 (M/49), 039 (F/28), 042 (F/28), 044 (M/58), 049 (F/52), 050 (M/20), 053 (F/39), 054 (M/23), 056 (M/34), 057 (M/53), 059 (F/44), 062 (F/23),

			065 (F/34), 066 (M/39), 067 (F/45), 068 (F/39), 069 (M/26), 070 (F/40), 074 (M/24), 075 (M/50), 077 (F/47), 080 (F/43), 084 (M/25), 089 (M/36), 094 (M/47), 101 (F/26), 102 (M/34), 105 (M/25), 106 (M/26), 111 (M/20), 114 (F/31), 115 (M/47), 120 (F/33), 121 (M/34), 125 (F/44), 128 (M/26), 130 (M/57), 134 (M/64), 135 (M/47), 138 (M/41), 147 (M/47), 151 (M/36), 153 (M/38), 156 (M/27), 158 (F/45), 161 (F/53), 162 (F/30), 163 (M/45), 164 (M/37), 168 (M/24), 171 (M/36), 173 (F/18), 174 (M/29), 175 (M/34), 176 (F/41), 177 (F/23), 184 (M/42), 186 (M/27), 189 (M/22), 193 (M/37), 195 (M/44), 196 (M/18), 203 (F/36), 204 (F/25), 232 (M/27), 234 (M/25), 236 (F/51), 240 (F/37), 247 (F/61), 251 (M/31), 260 (F/57), 268 (F/32), 275 (M/41), 286 (F/57), 292 (F/39), 297 (M/24), 299 (M/43)
MFG	538	97	002 (F/49), 003 (F/39), 006 (F/20), 015 (F/54), 020 (F/48), 022 (M/24), 023 (M/32), 026 (F/24), 030 (M/23), 032 (F/19), 033 (F/31), 034 (F/29), 036 (M/49), 039 (F/28), 042 (F/28), 045 (M/51), 049 (F/52), 051 (F/24), 053 (F/39), 054 (M/23), 056 (M/34), 057 (M/53), 059 (F/44), 060 (F/36), 062 (F/23), 063 (M/23), 065 (F/34), 066 (M/39), 067 (F/45), 069 (M/26), 070 (F/40), 074 (M/24), 075 (M/50), 076 (M/29), 077 (F/47), 081 (F/33), 084 (M/25), 089 (M/36), 098 (F/38), 102 (M/34), 105 (M/25), 106 (M/26), 114 (F/31), 115 (M/47), 121 (M/34), 127 (F/40), 129 (F/34), 130 (M/57), 131 (M/24), 135 (M/47), 136 (F/16), 137 (F/21), 142 (F/43), 147 (M/47), 148 (F/59), 149 (F/28), 151 (M/36), 153 (M/38), 155 (M/37), 156 (M/27), 158 (F/45), 159 (F/42), 162 (F/30), 163 (M/45), 164 (M/37), 166 (M/38), 168 (M/24), 172 (F/22), 175 (M/34), 177 (F/23), 178 (M/40), 186 (M/27),

			189 (M/22), 193 (M/37), 195 (M/44), 196 (M/18), 200 (M/25), 203 (F/36), 204 (F/25), 207 (F/39), 222 (F/20), 223 (F/42), 228 (F/58), 230 (F/56), 232 (M/27), 240 (F/37), 247 (F/61), 260 (F/57), 264 (F/52), 274 (F/44), 275 (M/41), 283 (F/29), 286 (F/57), 298 (F/24), 299 (M/43), 304 (F/33), 310 (M/20)

Table S3b. Number of electrodes in each node used in high-gamma power analysis in the categorized verbal free recall task. AI: anterior insula, PCC: posterior cingulate cortex, Pr: precuneus, mPFC: medial prefrontal cortex, dPPC: dorsal posterior parietal cortex, MFG: middle frontal gyrus.

Brain regions	**Number of electrodes (n)**	**Number of participants**	**Participant IDs (Gender/Age)**
AI	107	25	026 (F/24), 028 (F/27), 032 (F/19), 065 (F/34), 114 (F/31), 141 (F/44), 158 (F/45), 163 (M/45), 178 (M/40), 189 (M/22), 204 (F/25), 207 (F/39), 228 (F/58), 230 (F/56), 236 (F/51), 239 (M/27), 240 (F/37), 245 (M/30), 247 (F/61), 264 (F/52), 271 (M/37), 274 (F/44), 286 (F/57), 303 (F/62), 310 (M/20)
PCC/Pr	74	21	015 (F/54), 039 (F/28), 041 (M/34), 044 (M/58), 074 (M/24), 094 (M/47), 105 (M/25), 106 (M/26), 114 (F/31), 135 (M/47), 141 (F/44), 157 (M/22), 158 (F/45), 186 (M/27), 204 (F/25), 227 (M/32), 236 (F/51), 240 (F/37), 245 (M/30), 275 (M/41), 286 (F/57)
mPFC	116	33	026 (F/24), 029 (F/33), 036 (M/49), 039 (F/28), 041 (M/34), 056 (M/34), 060 (F/36), 074 (M/24), 075 (M/50), 106 (M/26), 107 (M/25), 114 (F/31), 119 (F/26), 130 (M/57), 131 (M/24), 141 (F/44), 163 (M/45), 167 (M/33), 180 (F/21), 181 (M/22), 187 (F/51), 189 (M/22), 202 (F/29), 204 (F/25), 212 (M/46), 222 (F/20), 228 (F/58), 245 (M/30), 247 (F/61), 271 (M/37), 274 (F/44), 275 (M/41), 303 (F/62)

dPPC	357	57	015 (F/54), 028 (F/27), 032 (F/19), 035 (F/45), 036 (M/49), 039 (F/28), 042 (F/28), 044 (M/58), 050 (M/20), 056 (M/34), 065 (F/34), 066 (M/39), 067 (F/45), 069 (M/26), 074 (M/24), 075 (M/50), 089 (M/36), 092 (M/44), 094 (M/47), 102 (M/34), 105 (M/25), 106 (M/26), 108 (F/23), 111 (M/20), 114 (F/31), 119 (F/26), 130 (M/57), 135 (M/47), 141 (F/44), 144 (M/53), 147 (M/47), 157 (M/22), 158 (F/45), 163 (M/45), 171 (M/36), 174 (M/29), 176 (F/41), 181 (M/22), 184 (M/42), 186 (M/27), 189 (M/22), 190 (F/57), 204 (F/25), 212 (M/46), 221 (M/57), 227 (M/32), 236 (F/51), 240 (F/37), 245 (M/30), 247 (F/61), 251 (M/31), 260 (F/57), 271 (M/37), 275 (M/41), 279 (F/57), 286 (F/57), 302 (M/48)
MFG	375	58	015 (F/54), 021 (M/38), 026 (F/24), 029 (F/33), 032 (F/19), 036 (M/49), 039 (F/28), 041 (M/34), 042 (F/28), 045 (M/51), 056 (M/34), 060 (F/36), 065 (F/34), 066 (M/39), 067 (F/45), 069 (M/26), 074 (M/24), 075 (M/50), 089 (M/36), 092 (M/44), 093 (M/24), 102 (M/34), 105 (M/25), 106 (M/26), 107 (M/25), 108 (F/23), 114 (F/31), 119 (F/26), 130 (M/57), 131 (M/24), 135 (M/47), 141 (F/44), 147 (M/47), 157 (M/22), 158 (F/45), 163 (M/45), 178 (M/40), 181 (M/22), 186 (M/27), 189 (M/22), 204 (F/25), 207 (F/39), 212 (M/46), 221 (M/57), 222 (F/20), 228 (F/58), 230 (F/56), 240 (F/37), 245 (M/30), 247 (F/61), 260 (F/57), 264 (F/52), 271 (M/37), 274 (F/44), 275 (M/41), 286 (F/57), 303 (F/62), 310 (M/20)

Table S3c. Number of electrodes in each node used in high-gamma power analysis in the paired associates learning verbal cued recall task. AI: anterior insula, PCC: posterior cingulate cortex, Pr: precuneus, mPFC: medial prefrontal cortex, dPPC: dorsal posterior parietal cortex, MFG: middle frontal gyrus.

Brain regions	Number of electrodes (n)	Number of participants	Participant IDs (Gender/Age)
AI	84	15	028 (F/27), 065 (F/34), 090 (F/52), 091 (M/28), 141 (F/44), 196 (M/18), 207 (F/39), 223 (F/42), 228 (F/58), 230 (F/56), 232 (M/27), 238 (M/27), 283 (F/29), 303 (F/62), 312 (M/21)
PCC/Pr	28	10	023 (M/32), 074 (M/24), 078 (F/2), 106 (M/26), 141 (F/44), 162 (F/30), 175 (M/34), 196 (M/18), 284 (F/32), 297 (M/24)
mPFC	78	20	036 (M/49), 056 (M/34), 060 (F/36), 074 (M/24), 082 (M/39), 097 (M/34), 106 (M/26), 121 (M/34), 130 (M/57), 131 (M/24), 141 (F/44), 142 (F/43), 175 (M/34), 196 (M/18), 202 (F/29), 212 (M/46), 223 (F/42), 228 (F/58), 263 (M/30), 303 (F/62)
dPPC	192	39	001 (F/48), 003 (F/39), 023 (M/32), 028 (F/27), 035 (F/45), 036 (M/49), 042 (F/28), 050 (M/20), 056 (M/34), 065 (F/34), 066 (M/39), 069 (M/26), 074 (M/24), 078 (F/22), 082 (M/39), 087 (M/51), 089 (M/36), 090 (F/52), 091 (M/28), 095 (F/35), 097 (M/34), 102 (M/34), 106 (M/26), 109 (F/43), 111 (M/20), 118 (M/33), 121 (M/34), 130 (M/57), 141 (F/44), 162 (F/30), 175 (M/34), 196 (M/18), 212 (M/46), 232 (M/27), 238 (M/27), 276 (M/28), 284 (F/32), 297 (M/24), 312 (M/21)
MFG	204	44	002 (F/49), 003 (F/39), 023 (M/32), 036 (M/49), 042 (F/28), 056 (M/34), 060 (F/36), 065 (F/34), 066 (M/39), 069 (M/26), 074 (M/24), 078 (F/22), 082 (M/39), 089 (M/36), 090 (F/52), 091 (M/28), 095 (F/35), 097 (M/34), 100 (F/43), 102 (M/34), 106 (M/26), 118 (M/33), 121 (M/34), 130 (M/57), 131 (M/24), 136 (F/16), 141 (F/44), 142 (F/43), 149 (F/28), 162 (F/30), 175 (M/34), 196 (M/18), 207 (F/39), 212 (M/46), 223 (F/42), 228 (F/58), 230 (F/56), 232 (M/27), 238 (M/27), 263 (M/30), 276 (M/28), 283 (F/29), 303 (F/62), 312 (M/21)

Table S3d. Number of electrodes in each node used in power spectral density (PSD) analysis in the water maze spatial memory task. AI: anterior insula, PCC: posterior cingulate cortex, Pr: precuneus, mPFC: medial prefrontal cortex, dPPC: dorsal posterior parietal cortex, MFG: middle frontal gyrus.

Brain regions	Number of electrodes (n)	Number of participants	Participant IDs (Gender/Age)
AI	59	11	026 (F/24), 030 (M/23), 032 (F/19), 033 (F/31), 049 (F/52), 052 (F/19), 054 (M/23), 062 (F/23), 065 (F/34), 114 (F/31), 124 (F/40)
PCC/Pr	89	21	006 (F/20), 010 (F/30), 015 (F/54), 018 (M/47), 023 (M/32), 024 (F/36), 030 (M/23), 034 (F/29), 041 (M/34), 044 (M/58), 049 (F/52), 051 (F/24), 054 (M/23), 062 (F/23), 064 (M/56), 074 (M/24), 077 (F/47), 101 (F/26), 106 (M/26), 114 (F/31), 124 (F/40)
mPFC	77	17	014 (F/47), 018 (M/47), 025 (F/19), 026 (F/24), 034 (F/29), 041 (M/34), 049 (F/52), 051 (F/24), 052 (F/19), 056 (M/34), 060 (F/36), 062 (F/23), 074 (M/24), 075 (M/50), 077 (F/47), 106 (M/26), 114 (F/31)
dPPC	226	36	001 (F/48), 006 (F/20), 010 (F/30), 014 (F/47), 015 (F/54), 018 (M/47), 019 (F/34), 023 (M/32), 024 (F/36), 025 (F/19), 030 (M/23), 032 (F/19), 033 (F/31), 042 (F/28), 044 (M/58), 049 (F/52), 050 (M/20), 052 (F/19), 054 (M/23), 056 (M/34), 062 (F/23), 064 (M/56), 065 (F/34), 066 (M/39), 067 (F/45), 068 (F/39), 069 (M/26), 074 (M/24), 075 (M/50), 077 (F/47), 089 (M/36), 101 (F/26), 106 (M/26), 114 (F/31), 124 (F/40), 177 (F/23)
MFG	147	33	006 (F/20), 014 (F/47), 015 (F/54), 019 (F/34), 021 (M/38), 023 (M/32), 025 (F/19), 026 (F/24), 030 (M/23), 032 (F/19), 033 (F/31), 034 (F/29), 041 (M/34), 042 (F/28), 045 (M/51), 049 (F/52), 051 (F/24), 052 (F/19), 054 (M/23), 056 (M/34), 060 (F/36), 062 (F/23), 065 (F/34), 066 (M/39), 067 (F/45), 069 (M/26), 074 (M/24),

			075 (M/50), 077 (F/47), 089 (M/36), 106 (M/26), 114 (F/31), 177 (F/23)